Understanding anomalous delays in a model of intracellular calcium dynamics

Emily Harvey, Vivien Kirk, Hinke M. Osinga, James Sneyd, and Martin Wechselberger

Related Articles

The effects of thermal stimuli on intracellular calcium change and histamine releases in rat basophilic leukemia mast cells
J. Appl. Phys. 111, 104701 (2012)

Structural properties of rutile TiO2 nanoparticles accumulated in a model of gastrointestinal epithelium elucidated by micro-beam x-ray absorption fine structure spectroscopy
Appl. Phys. Lett. 100, 214101 (2012)

Physical aspects of biological activity and cancer
AIP Advances 2, 011207 (2012)

Enhanced endocytosis of nano-curcumin in nasopharyngeal cancer cells: An atomic force microscopy study
Appl. Phys. Lett. 99, 163706 (2011)

Ab initio calculation of the potential of mean force for dissociation of aqueous Ca–Cl
J. Chem. Phys. 134, 204510 (2011)

Additional information on Chaos

Understanding anomalous delays in a model of intracellular calcium dynamics

Emily Harvey,[1] Vivien Kirk,[1] Hinke M. Osinga,[2] James Sneyd,[1] and Martin Wechselberger[3,a]

[1]*Department of Mathematics, University of Auckland, Private Bag, 92019 Auckland, New Zealand*
[2]*Department of Engineering Mathematics, University of Bristol, Bristol BS8 1TR, United Kingdom*
[3]*School of Mathematics and Statistics, University of Sydney, New South Wales 2006, Australia*

In many cell types, oscillations in the concentration of free intracellular calcium ions are used to control a variety of cellular functions. It has been suggested [J. Sneyd *et al.*, "A method for determining the dependence of calcium oscillations on inositol trisphosphate oscillations," Proc. Natl. Acad. Sci. U.S.A. **103**, 1675–1680 (2006)] that the mechanisms underlying the generation and control of such oscillations can be determined by means of a simple experiment, whereby a single exogenous pulse of inositol trisphosphate (IP$_3$) is applied to the cell. However, more detailed mathematical investigations [M. Domijan *et al.*, "Dynamical probing of the mechanisms underlying calcium oscillations," J. Nonlinear Sci. **16**, 483–506 (2006)] have shown that this is not necessarily always true, and that the experimental data are more difficult to interpret than first thought. Here, we use geometric singular perturbation techniques to study the dynamics of models that make different assumptions about the mechanisms underlying the calcium oscillations. In particular, we show how recently developed canard theory for singularly perturbed systems with three or more slow variables [M. Wechselberger, "A propos de canards (Apropos canards)," Preprint, 2010] applies to these calcium models and how the presence of a curve of folded singularities and corresponding canards can result in anomalous delays in the response of these models to a pulse of IP$_3$. © *2010 American Institute of Physics*. [doi:10.1063/1.3523264]

Oscillations in the concentration of cytoplasmic free calcium are a signaling mechanism in practically every cell type and control a wide variety of cellular functions, from secretion and movement to cell differentiation and gene expression.[3] It is thus important to understand the mechanisms underlying the generation and control of such oscillations. Previous work has shown that calcium oscillations often arise as a result of one of the two principal mechanisms: either *class I* mechanisms, where oscillations occur as a result of calcium feedback on the inositol trisphosphate (IP$_3$) receptor, or *class II* mechanisms, where calcium affects the rate of production or degradation of IP$_3$, leading to feedback on the release of calcium. It has been claimed[22] that a simple experiment (a single exogenous pulse of IP$_3$) is able to distinguish between whether or not calcium oscillations in a cell are a result principally of a class I or a class II mechanism. However, more detailed mathematical studies of these models[7] have shown that the situation is more complex than appeared at first, and there are situations in which a class I model can look remarkably like a class II model, making the interpretation of the experimental data ambiguous and difficult. Here, we perform a detailed mathematical study of class I and class II models, investigate how they respond to a pulse of IP$_3$, and provide a detailed explanation of why class I and class II models cannot necessarily be easily distinguished by the IP$_3$ pulse experiment. It turns out that this is related to the phenomenon of canards in systems with three slow variables, the theory of which has been developed recently.[25]

I. INTRODUCTION

Calcium is one of the main secondary signaling messengers in living cells.[3] Changes in calcium concentration usually take the form of oscillations, in which the free cytoplasmic calcium concentration alternately rises and falls. In most cells, it is believed that the signal is encoded in the frequency of the oscillation, although in some cells the amplitude of the oscillations is known to be important as well.[13]

There is general agreement over the first steps of the process that results in calcium oscillations:[13] binding of an agonist to a cell-surface receptor initiates a series of reactions that ends in the formation of the intracellular second messenger, inositol (1,4,5)-trisphosphate (IP$_3$), which opens IP$_3$ receptors (which are also calcium channels) on the membrane of the endoplasmic reticulum (ER), leading to the release of calcium from that internal store. Oscillations in the cytoplasmic calcium concentration occur as calcium is alternately released from, and pumped into, the ER.

The exact mechanisms that cause such cyclical release and re-uptake remain controversial. There are two principal hypotheses: *class I models* claim that the oscillations occur as a result of calcium feedback on the IP$_3$ receptor (IPR).[22] Since calcium can activate the IPR quickly, release of

---
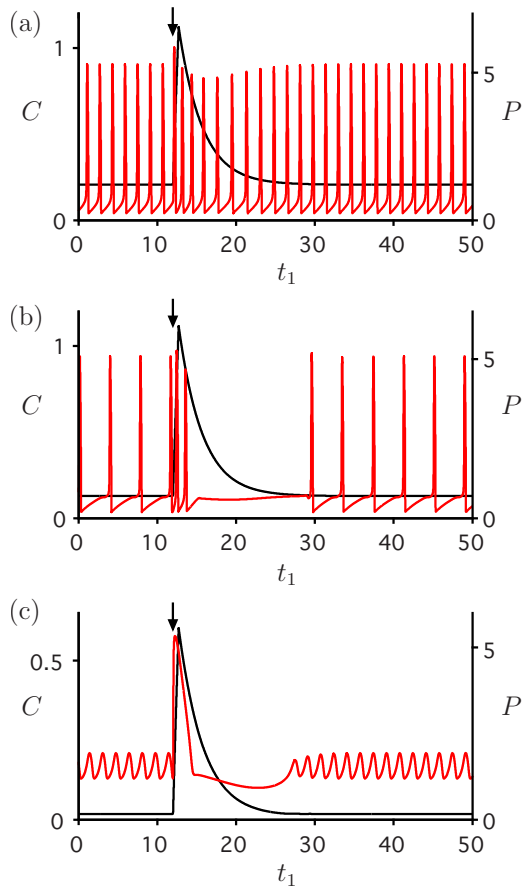a)Author to whom correspondence should be addressed.

FIG. 1. (Color online) Responses of the Atri model (1) with $\epsilon=0.01$ to IP$_3$ pulses. The IP$_3$ pulse is applied at the time indicated by the arrow, with the explicit form of the pulse given by Eq. (2), assuming that any transients have died out before the time trace is started. Each panel shows the time series of the concentrations C of calcium (red curve) and P of IP$_3$ (black curve). Panel (a) is for class I with $\alpha=0$, $\hat{\tau}=0.48$ ($\tau=2$) for $\hat{\nu}=0.40$ ($\nu=0.96$) and other parameter values as in Table I. Panel (b) is also for class I, as in panel (a) except with $\hat{\nu}=0.233$ ($\nu=0.56$). Panel (c) is for class II with $\alpha=1$, $\hat{\tau}=0$ ($\tau=0$) for $\hat{\nu}=0.417$ ($\nu=1.00$).

calcium from the ER is a positive feedback process. However, on a slower time scale, calcium also inactivates the IPR, thus giving a slower negative feedback. It is well known from many models[13] that fast positive feedback followed by slower negative feedback can generate oscillations. However, the biochemistry of calcium oscillations is far more complex than merely feedback on the IPR. Indeed, calcium itself affects the rates of production and degradation of IP$_3$, leading again to positive and negative feedback on the release of calcium. This second feedback loop is incorporated in *class II models* and is the principal mechanism underlying oscillations in some cell types.[22]

However, in real cells, both class I and class II mechanisms will usually occur, in which case one has to use a *hybrid model* that includes both mechanisms. One of the important current questions in the study of calcium dynamics is whether, in each cell type, both mechanisms are equally important, or whether one mechanism, class I or class II, dominates and, hence, drives the oscillations.

One possible way to distinguish between class I and class II mechanisms was introduced in Ref. 22. There, it was

shown that in a variety of class I models, an exogenous pulse of IP$_3$ causes a temporary increase in oscillation frequency, while in class II models, an identical pulse of IP$_3$ causes a phase lag, with the next peak occurring after a delay. These types of responses are illustrated in Figs. 1(a) and 1(c), respectively, with time series of the concentrations of calcium and IP$_3$ generated from a representative intracellular calcium model known as the *Atri model*,[1,7] system (1) as defined below in Sec. I A.

The model predictions were tested in two cell types, namely, in mouse pancreatic acinar cells and mouse airway smooth muscle cells.[22] The authors concluded that calcium oscillations generated by cholecystokinin in pancreatic acinar cells are the result of a class II mechanism, while calcium oscillations generated by methacholine in mouse airway smooth muscle are the result of a class I mechanism.

Unfortunately, the story is not as simple as presented in Ref. 22. As reported in Ref. 7, under certain conditions, a class I model can respond to an IP$_3$ pulse by exhibiting a small number of faster oscillations, followed by a long delay, before recovering to the initial oscillatory pattern. This is a highly nonintuitive result: in class I models the oscillation frequency is an increasing function of the IP$_3$ concentration (assuming that transients have died away), and thus a temporary increase in the IP$_3$ concentration might be expected to lead to a temporary increase in oscillation frequency, not to a long delay. Although this is usually what happens, sometimes the pulse in IP$_3$ causes the response described above, i.e., a small number of faster oscillations, followed by a long delay before oscillations appear again. A specific example of such a response can be seen in Fig. 1(b). We term this response an *anomalous delay*. The occurrence of anomalous delays under certain circumstances creates problems for the interpretation of the experimental results. If a class I model can sometimes respond like a class II model, then how can the two model types be distinguished using pulses of IP$_3$?

A. Multiple time scales in a representative model

A first step toward a better understanding of the model dynamics is presented in our recent work.[11] Based on geometric singular perturbation theory (GSPT),[5,10,12,23,26] we showed in that paper that the intrinsic dynamics of models of intracellular calcium dynamics is mainly controlled by distinct time scales describing the (slow or fast) evolution of the model variables relative to each other. This inherent multiple-time-scale structure provides us with a simple necessary condition for class I and class II dynamics by calculating a dimensionless quantity $\epsilon \ll 1$ representing the ratio of the different time scales involved.

This is most easily illustrated using a representative model, the Atri model,[1,7] which we will use as an example throughout this paper, and which has the following dimensionless form:[11]

$$\begin{cases} \epsilon \dfrac{dC}{dt_1} = \bar{J}_{\text{release}} - \bar{J}_{\text{serca}} + \epsilon(\bar{J}_{\text{in}} - \bar{J}_{\text{pm}}) = f(C, C_t, r, P, \epsilon) \\[2mm] \dfrac{dC_t}{dt_1} = \bar{J}_{\text{in}} - \bar{J}_{\text{pm}} = g_1(C) \\[2mm] \dfrac{dr}{dt_1} = \dfrac{1}{\hat{\tau}}\left(\dfrac{k_2^2}{k_2^2 + Q_c^2 C^2} - r \right) = g_2(C, r) \\[2mm] \dfrac{dP}{dt_1} = \hat{\nu}\left(1 - \dfrac{\alpha}{1 + \dfrac{Q_c C}{k_4}} \right) - \hat{\beta}P = g_3(C, P), \end{cases}$$

$$(1)$$

with dimensionless fluxes

$$\bar{J}_{\text{release}} = \dfrac{k_{\text{flux}}\gamma Q_c}{V_p}\left(\mu_0 + \mu_1 \left(\dfrac{P}{P + \dfrac{k_\mu}{Q_p}} \right) \right) r \left(b + V_1 \dfrac{C}{C + \dfrac{k_1}{Q_c}} \right)$$
$$\times (C_t - (1 + 1/\gamma)C),$$

$$\bar{J}_{\text{serca}} = \dfrac{V_e}{V_p} \dfrac{C}{C + \dfrac{k_e}{Q_c}},$$

$$\bar{J}_{\text{pm}} = \dfrac{C^2}{C^2 + \dfrac{k_p^2}{Q_c^2}},$$

$$\bar{J}_{\text{in}} = \dfrac{\alpha_1}{V_p} + \dfrac{\alpha_2}{V_p} \dfrac{Q_p \hat{\nu}}{\hat{\beta}}.$$

The four variables are the nondimensionalized calcium concentration C in the cytoplasm (reference scale is $Q_c = 1.0 \ \mu M$), the nondimensionalized total calcium concentration C_t in the cell (again, reference scale is $Q_c = 1.0 \ \mu M$), the nondimensionalized IP$_3$ concentration P in the cytoplasm (reference scale is $Q_p = 10.0 \ \mu M$), and the fraction r of IPRs that have not been inactivated by calcium. The values of the parameters used in Eq. (1) are the same as those in Ref. 7 and given in Table I; we work here with the dimensionless parameters $\hat{\tau} = \tau \delta V_p / Q_c$, $\hat{\nu} = \nu Q_c / (Q_p \delta V_p)$, $\hat{\beta} = \beta Q_c / (\delta V_p)$, and $\epsilon = \delta \ll 1$, which is the singular perturbation parameter. The parameter $\hat{\nu}$ is a scaled version of the maximal rate ν of IP$_3$ formation. Experimentally, ν is relatively easily manipulated as it is directly related to the concentration of agonist applied to the cell. We use $\hat{\nu}$ as the primary bifurcation parameter, but also report our results in terms of ν for ease of comparison with earlier work on the Atri model.[7]

With the choice of model parameter values as given in Table I, the dynamics of C is significantly faster than the dynamics of C_t, as is consistent with previous theoretical and experimental works.[21] As argued in Ref. 11, the parameters $\hat{\beta}$ and $\hat{\nu}$ are $O(1)$ in the parameter domain of interest, so P is a slow variable compared with C. The dynamics of r, the inactivation of the IP$_3$ receptor, is of order $O(1/\hat{\tau})$. If $\hat{\tau} = O(1)$, then r is a slow variable. On the other hand, if

TABLE I. Values of parameters for the Atri model (1), which are the same as the values used in Ref. 7. All substrate concentrations are concentrations per liter cytosol, i.e., $\mu M \equiv \mu M / (\text{liter cytosol})$.

Parameter	Value
b	0.111
δ	0.01
γ	5.405
μ_0	0.567
μ_1	0.433
V_1	0.889
k_2	0.7 μM
k_4	1.1 μM
k_p	0.4 μM
k_e	0.06 μM
k_1	1.1 μM
k_μ	4.0 μM
k_{flux}	6.0 s^{-1}
V_p	24.0 μM s^{-1}
V_e	20.0 μM s^{-1}
α_1	1.0 μM s^{-1}
α_2	0.2 s^{-1}
β	0.8 s^{-1}

$\hat{\tau} = O(\epsilon)$ or less, then r is a fast variable. These two cases have an interpretation in terms of the class I and class II models as discussed before.

Class I models require a slow negative feedback on the IP$_3$ receptor, which is modeled by r. Therefore, $\hat{\tau} = O(1)$ is a necessary condition and we define a class I model as Eq. (1) with $\alpha = 0$, i.e., no calcium feedback on the IP$_3$ production, and $\hat{\tau} = O(1)$. This leads to a model with one fast (C) and three slow variables (C_t, r, P). Note that the dynamics of the third slow variable P is decoupled from the others. On the other hand, class II models abolish the slow negative feedback on the IP$_3$ receptor via a fast (instantaneous) response to calcium concentration in the r-dynamics but include calcium feedback on the IP$_3$ production. Hence, we define a class II model as Eq. (1) with $\alpha \neq 0$ and $0 < \hat{\tau} \ll 1$, which leads to a model with two fast (C, r) and two slow variables (C_t, P). The hybrid Atri model is then defined as Eq. (1) with $\alpha \neq 0$ and $\hat{\tau} = O(1)$ or less, and may have either two or three slow variables, depending on the order of $\hat{\tau}$.

In all these cases (class I, class II, or hybrid), the Atri model (1) has at least two slow variables, which makes our geometric singular perturbation analysis presented in Ref. 11 significantly different from the presentation in Ref. 7 where they only identified one slow variable (C_t). In particular, we were able to explain mixed-mode oscillations (MMOs)[4] observed in class I and class II via canard theory,[5,6,26] and we also identified the necessary time-scale criterion for the r-dynamics to distinguish class I and class II models.

B. The focus of this work

In this paper, we go a step further with our analysis and consider the response to a pulse of IP$_3$ in class I, class II, and hybrid forms of the Atri model. We use GSPT[5,10,12,23,25,26] to investigate the mechanisms underlying the different pulse responses and, in particular, to explain the anomalous delays

seen in, for example, Fig. 1(b). In our numerical simulations, we follow Ref. 7 and model the pulsing process using the time-dependent function,

$$S(t_1) = \hat{M}H(t_1 - t_0)H(t_0 + \Delta - t_1), \qquad (2)$$

which is added to the right-hand side of the equation for P in Eq. (1). Here, $\hat{M}$ denotes the pulse magnitude and H is the Heaviside function,

$$H(x) = \begin{cases} 0 & \text{if } x < 0 \\ 1 & \text{if } x \geq 0. \end{cases}$$

The pulse is applied at time t_0 and has duration Δ; we used $\hat{M} = 8.33\overline{3}$, $t_0 = 12$, and $\Delta = 0.72$ throughout, which are the values used in Ref. 7, after nondimensionalization.

We want to point out that the results obtained in Ref. 11 for the class I model are not sufficient to predict the pulsed dynamics for the class I model or the dynamics of the hybrid model in the case $\hat{\tau} = O(1)$; in these two cases, a model reduction to two slow variables is not possible and we must study the full four-dimensional system (1) with three slow variables to understand rigorously the observed pulsing behavior.

Section II presents the analysis of the class I Atri model. Although this system has three slow variables, we show that it has geometric structures similar to those found in other biophysical models with two slow variables.[9,15,19,20,24] We identify specific geometric objects (so-called *folded invariant manifolds* and *canards*,[23,25,26] as defined in Sec. II A) that are responsible for the anomalous delays observed in certain parameter regimes of the pulsed class I Atri model and explain why these mechanisms for delay could not occur if there were only two slow variables in the model. In particular, we identify two major types of anomalous delays caused by two different mechanisms. These results provide the first application of recent work of Wechselberger,[25] which extends canard theory to systems with three (or more) slow variables.

The analysis for the class II model is done in Sec. III. We show in Sec. IV that the hybrid model can exhibit dynamics similar to either the class I or class II models, and that the presence or absence of anomalous delays in this case can be understood just as in the class I and class II cases. The relation between earlier work on pulse responses reported in Ref. 7 and the results presented here is discussed in detail in Sec. V, where we also summarize our results.

II. DYNAMICS OF THE CLASS I ATRI MODEL

The class I Atri model, for which $\alpha = 0$ and $\hat{\tau} = O(1)$ in Eq. (1), has one fast variable, namely, C, and three slow variables, namely, C_t, r, and P. Since $\alpha = 0$, the $\dot{P}$-equation decouples from the other variables and P evolves monotonically to its equilibrium value $P = \hat{v}/\hat{\beta}$. If one is primarily

interested in the long-term dynamics of the class I Atri model, then it suffices to study the three-dimensional slice $\{P = \hat{v}/\hat{\beta}\}$ of the (C, C_t, r, P)-space because all orbits will eventually evolve to this submanifold of phase space. This approach was taken in Ref. 11 to study the unpulsed dynamics, and we give a brief summary in Sec. II A including basic concepts from GSPT.[5,6,25,26]

In order to understand the transient response to pulsing of IP$_3$, analysis of the full four-dimensional system is necessary. We present these new results about the pulsed class I Atri model in Sec. II B, where we also describe two mechanisms that explain the anomalous delays sometimes seen in this case.

We use $\hat{\tau} = 0.48$ ($\tau = 2.0$) throughout for the numerical illustrations of the class I Atri model. Qualitatively similar results are obtained for other choices of $\hat{\tau}$ that are $O(1)$.

A. Class I dynamics in the absence of pulsing

If we restrict our attention to the slice $\{P = \hat{v}/\hat{\beta}\}$, then the class I Atri model becomes a system with one fast and two slow variables. The dynamics of such a three-dimensional system can be analyzed using the established methods from GSPT.[5,6,26] However, we prefer to summarize the results in Ref. 11 about the unpulsed class I Atri model in the context of the full four-dimensional phase space because this facilitates the extension to the pulsed case.

The dynamics of singularly perturbed systems such as the Atri model (1) frequently consists of a mix of slow and fast motions, with the prototypical example being a relaxation oscillation (RO), i.e., a periodic motion consisting of long periods of small changes interspersed with short periods of large changes in the (fast) state variables. As $\epsilon \to 0$, the corresponding trajectory converges during slow motions to solutions of the singular limit system of Eq. (1),

$$\begin{cases} 0 = f(C, C_t, r, P, 0) \\ \dfrac{dC_t}{dt_1} = g_1(C) \\ \dfrac{dr}{dt_1} = g_2(C, r) \\ \dfrac{dP}{dt_1} = g_3(C, P), \end{cases} \qquad (3)$$

which is a differential algebraic system called the *reduced problem*. Here, the algebraic constraint $f(C, C_t, r, P, 0) = 0$ defines a three-dimensional (hyper)surface S_0, which is the phase space for the three slow variables (C_t, r, P). As described in Ref. 11, S_0 is given (in the physiological relevant domain) as a graph over (C, r, P)-space, i.e., $S_0 = \{(C, C_t, r, P) \in \mathbb{R}_+^4 : C_t = C_t(C, r, P)\}$, where
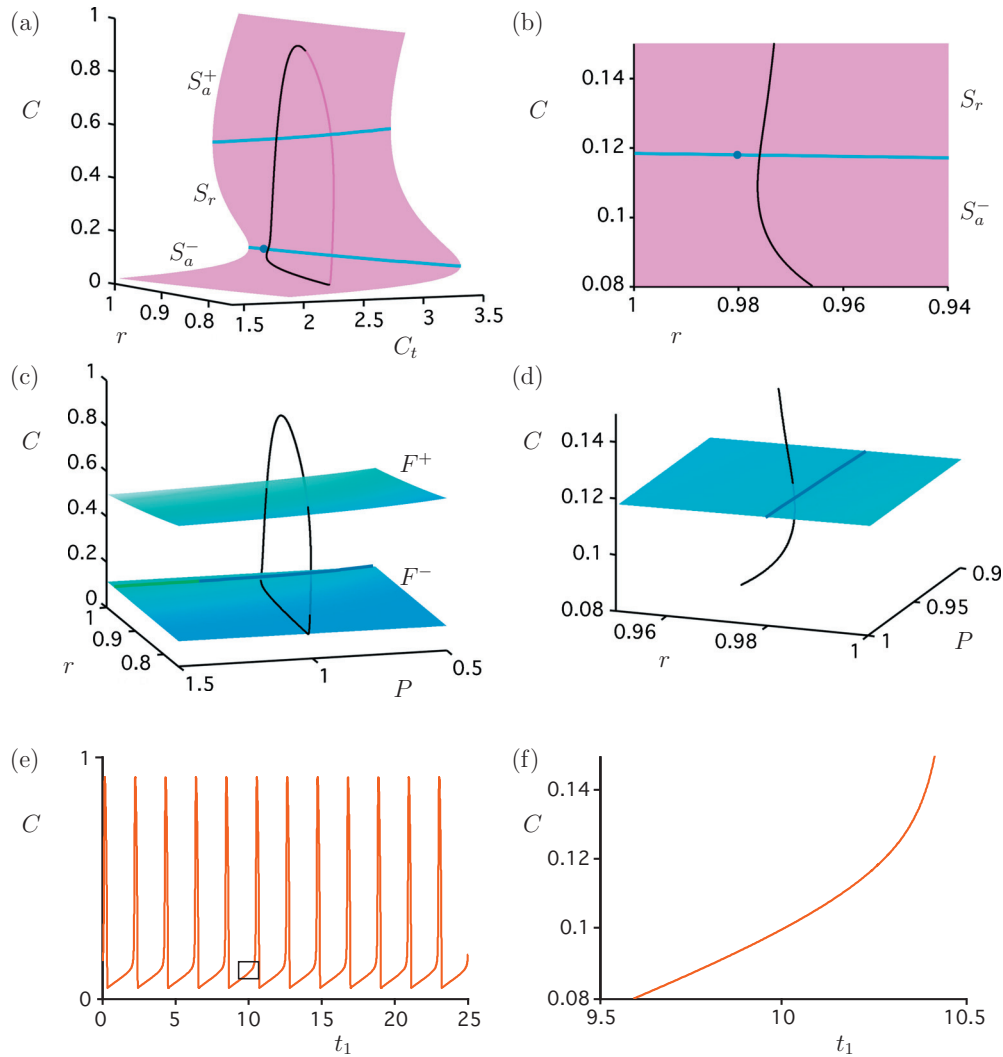
FIG. 2. (Color) Example of an attracting RO (black curve) for the class I Atri model with $\epsilon=0.01$ and $\hat{v}=0.317$ ($\nu=0.76$). The slow and fast segments of the RO can be explained using the critical manifold, as explained in the text. Panel (a) shows the intersection of the critical manifold (pink surface) with the slice in (C,r,C_t)-coordinates, where $P=\hat{v}/\hat{\beta}=0.95$ is fixed at its equilibrium value. The blue curves are the intersections of the fold surfaces with the slice and the blue dot marks the folded-focus singularity that occurs for this value of P. Panel (b) is an enlargement showing the passage of the RO past the folded-focus singularity projected onto the (r,C)-plane. Panel (c) shows the projection onto (C,r,P)-coordinates with an enlargement near the folded focus shown in panel (d). The blue surfaces are the fold surfaces $F^{\pm}$; on these surfaces the C_t-coordinate appears as a color gradient (light to dark as C_t increases). The green and dark-blue curve is the locus of folded singularities; blue indicates a folded focus, green indicates a folded node, consistent with the color coding of singularities in Fig. 3. Panel (e) with corresponding enlargement in panel (f) shows the time series for C corresponding to the RO.

$$C_t(C,r,P) = (1+1/\gamma)C + \dfrac{\dfrac{C}{C+\dfrac{k_e}{Q_c}}}{\dfrac{k_{\mathrm{flux}}\gamma Q_c}{V_e}\left(\mu_0 + \mu_1\left(\dfrac{P}{P+\dfrac{k_\mu}{Q_p}}\right)\right)\left(r\left(b+V_1\dfrac{C}{C+\dfrac{k_1}{Q_c}}\right)\right)}. \tag{4}$$

This graph representation of the critical manifold can partially be seen in Fig. 2(a), which shows S_0 for $\hat{v}=0.317$ ($\nu=0.76$) restricted to the slice $\{P=\hat{v}/\hat{\beta}\}$ in (C,r,C_t)-space. The critical manifold is cubic shaped and this is also the case for other values of P. Hence, there are two *fold surfaces*,

$F^{\pm}=\{(C,C_t,r,P)\in S_0 : f_C(C,C_t,r,P)=0\}$, where $f_C=\partial f/\partial C$, in the full four-dimensional phase space, as shown in Fig. 2(c) in projection onto (C,r,P)-space. The color gradient on these surfaces indicates the value of C_t, ranging from 2.1 (light) to 3.2 (dark). The fold surfaces $F^{\pm}$ separate S_0 into

three three-dimensional sheets, $S_a^{\pm}$ and S_r; the outer two sheets, $S_a^{\pm}$, are attracting and the inner sheet, S_r, is repelling. Thus, $S_0 = S_a^{-} \cup F^{-} \cup S_r \cup F^{+} \cup S_a^{+}$. Note that the objects in Figs. 2(a) and 2(c) are viewed from below, that is, the lower fold curve is closer to the viewer than the upper fold curve.

During fast motions, the trajectory of a RO converges to solutions of the *layer problem*, which is obtained by first switching to the fast time scale $t_2 = t_1/\epsilon$ in Eq. (1) and then taking the singular limit $\epsilon \to 0$, which gives

$$\begin{cases} \dfrac{dC}{dt_2} = f(C, C_t, r, P, 0) \\ \dfrac{dC_t}{dt_2} = \dfrac{dr}{dt_2} = \dfrac{dP}{dt_2} = 0. \end{cases} \tag{5}$$

Hence, the layer problem is a simple one-dimensional system for the evolution of the fast variable C, while the slow variables (C_t, r, P) are constant. Note that the three-dimensional manifold S_0, the phase space of the reduced problem (3), is a manifold of equilibria for the layer problem (5) and defines the interface between the two subsystems. The motion toward $S_a^{\pm}$ or away from S_r in the layer problem is along one-dimensional *fast fibers*. In the singular limit, switching between slow and fast motion of a RO happens at the fold surfaces $F^{\pm}$.

Figure 2 clearly shows the power of GSPT, namely, the ability to concatenate solution segments of the lower-dimensional limiting problems, the one-dimensional layer (5) and the three-dimensional reduced problem (3), to obtain an approximate solution of the full four-dimensional model (1). Starting from F^{-} at relatively low C-values, near the blue dot in Fig. 2(a), the RO makes an almost vertical jump away from S_0, with a corresponding sharp peak in the time series in Fig. 2(e). As soon as the orbit reaches the attracting sheet S_a^{+} of S_0, the motion becomes slow again and follows S_0 back to the other fold surface F^{+}, after which another near-vertical jump occurs to the other attracting sheet S_a^{-} of S_0. In Fig. 2(c), we cannot see the attracting sheets $S_a^{\pm}$, but we can clearly distinguish the near-vertical jumps in the fast C-direction. Observe how the orbit passes the upper fold surface F^{+} in Fig. 2(c) on its way to S_a^{+}. This is not a true intersection but appears to be so only due to the projection of four-dimensional phase space. A similar observation can be made at the lower fold surface F^{-} in Fig. 2(c).

In the Atri model, the layer problem is particularly simple since it is only one dimensional, and so we focus solely on analyzing the three-dimensional reduced problem (3). By definition, the reduced vector field has to be in the tangent bundle of the critical manifold S_0. As described in Eq. (4), S_0 is given as a graph over (C, r, P)-space, i.e., $C_t = C_t(C, r, P)$. This graph representation of S_0 provides the opportunity to study the reduced flow (3) in the single (C, r, P)-chart. Taking the total time derivative of $f(C, C_t, r, P, 0) = 0$ defines a vector field for C that is constrained to the tangent bundle of S_0 and leads to the reduced problem projected onto the base (C, r, P) given by

$$\begin{cases} -f_C \dfrac{dC}{dt_1} = f_{C_t} g_1 + f_r g_2 + f_P g_3 \\ \dfrac{dr}{dt_1} = -g_2 \\ \dfrac{dP}{dt_1} = -g_3, \end{cases} \tag{6}$$

where $(C, C_t, r, P) \in S_0$ and $f_C = \partial f/\partial C$, $f_{C_t} = \partial f/\partial C_t$, etc. This system is singular along the fold surfaces $F^{\pm}$, where $f_C = 0$. To understand the reduced flow completely, we rescale time by the factor $-f_C$, which gives the *desingularized problem*

$$\begin{cases} \dot{C} = f_{C_t} g_1 + f_r g_2 + f_P g_3 \\ \dot{r} = -f_C g_2 \\ \dot{P} = -f_C g_3, \end{cases} \tag{7}$$

where the overdot denotes, for convenience, differentiation with respect to the new rescaled time. The reduced flow is equivalent to the desingularized flow up to a time parametrization change on the repelling sheet S_r where $f_C > 0$, i.e., one only has to reverse the direction of the desingularized flow on S_r to obtain the corresponding reduced flow. We distinguish two types of singularities in the desingularized problem (7):

- *Ordinary singularities* are defined by $g_1 = g_2 = g_3 = 0$ away from the fold surface, i.e., $f_C \neq 0$.
- *Folded singularities* are defined by $f_C = 0$ and $f_{C_t} g_1 + f_r g_2 + f_P g_3 = 0$, and represent a one-dimensional submanifold of singularities on the fold surface $f_C = 0$.

Ordinary singularities correspond generically to isolated equilibrium points of the reduced problem (6) [respectively Eq. (3)]. Here, we have a single equilibrium that is a stable node on the lower sheet S_a^{-} for $0 < \hat{\nu} < 0.144$ ($0 < \nu < 0.345$), a saddle on the middle sheet S_r for $0.144 < \hat{\nu} < 3.34$ ($0.345 < \nu < 8.02$), and again a stable node but on the upper sheet S_a^{+} for $\hat{\nu} > 3.34$ ($\nu > 8.02$). GSPT predicts that for sufficiently small $\epsilon > 0$, these hyperbolic equilibria (away from the fold surfaces $F^{\pm}$) persist as true equilibria of the full system (1). In the case of a stable node, this equilibrium corresponds to the only stable attractor of the system.

In the case of the (unstable) saddle equilibria, there exist stable attractors other than equilibria and the folded singularities become important objects in determining these attractors. It turns out that at the values of $\hat{\nu}$ of interest, only one of the two fold surfaces of S_0 contains such folded singularities, namely, the fold surface F^{-} with the lowest C-values, as indicated in Fig. 2(c). These folded singularities all have one zero eigenvalue since there is a curve of folded singularities. The corresponding eigenvector of each of these folded singularities is tangent to the curve of folded singularities. The other two eigenvalues vary as we move along the curve of folded singularities. Following the general canard theory developed in Ref. 25 and by analogy with canard theory for the case of two slow variables,[2,23,26] we classify these singularities according to the signs of their nonzero eigenvalues. A folded singularity with two negative real eigenvalues (and
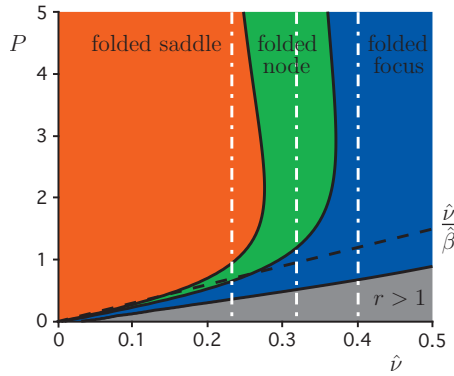
FIG. 3. (Color) Classification of folded singularities on the fold surface F^- of S_0 in the class I Atri model for a range of values of $\hat{\nu}$. For each $\hat{\nu}$, there exists a curve of folded singularities parametrized by P. The type of the folded singularities are indicated by the colors red, green, and blue, for folded saddle, folded node, and folded focus, respectively. The gray shaded region consists only of folded singularities with $r > 1$, which is unphysical. The equilibrium value of $P = \hat{\nu}/\hat{\beta}$ (black dashed line) indicates at which folded singularity the attractor passes the fold surface. The white dashed lines indicate the values of $\hat{\nu}$ used for Figs. 6, 7, and 9 (from right to left, respectively).

one zero eigenvalue) is called a *folded node*, a singularity with two real eigenvalues of opposite sign is called a *folded saddle*, and a singularity with a complex conjugate pair of eigenvalues with nonzero real part is called a *folded focus*. Figure 3 shows the types of folded singularities seen in the class I Atri model for a range of $\hat{\nu}$-values by assigning a color to the P-coordinate associated with each singularity; we color folded saddles red, folded nodes green, and folded foci blue.

Note that folded singularities do not correspond to the equilibria of the reduced flow (6). In the case of a folded saddle or folded node, the role of the folded singularity is to provide a mechanism by which orbits of the reduced flow on the outer sheet S_a^- may reach the folded singularity in finite time and then cross to the repelling inner sheet S_r. In the case of a folded node, there is an associated sectorial region of phase space, known as the *funnel*, in which trajectories are attracted to the folded node and can pass from S_a^- to S_r. For $\epsilon \neq 0$, this leads to local oscillatory behavior, as shown in Figs. 4(b), 4(d), and 4(f), due to *canards of folded node type* (see, e.g., Refs. 23, 25, and 26 for theoretical background).

The dynamics of the full (i.e., nonsingular) unpulsed class I system can now be understood in terms of these geometric structures. Since we are not interested in the transient behavior in the unpulsed case, the relevant folded singularity is that which occurs at the equilibrium value of P for the $\hat{\nu}$ value of interest; this $\hat{\nu}$-dependent line of singularities is indicated by the dashed black line in Fig. 3. We find that the singularity at $P = \hat{\nu}/\hat{\beta}$ is a folded saddle for $\hat{\nu} \in [0.0, 0.144]$ ($\nu \in [0.0, 0.345]$), a folded node for $\hat{\nu} \in [0.144, 0.259]$ ($\nu \in [0.345, 0.623]$), and a folded focus for $\hat{\nu} > 0.259$ ($\nu > 0.623$).

GSPT predicts that for sufficiently small $\epsilon > 0$, the attractor in the region with $\hat{\nu} < 0.144$ ($\nu < 0.345$) and $\hat{\nu} > 3.34$ ($\nu > 8.02$) is the stable node equilibrium (as explained above). In the case $3.34 > \hat{\nu} > 0.259$, we have a

saddle on the repelling inner sheet S_r and a folded focus on F^-. GSPT predicts in this case a stable RO as the attractor. The equilibrium value $P = \hat{\nu}/\hat{\beta}$ for the case shown in Fig. 2 lies in the blue region of Fig. 3 and the enlargements in Figs. 2(b), 2(d), and 2(f) show that the periodic orbit is, indeed, a RO.

In the case $0.114 < \hat{\nu} < 0.259$, there is a saddle on the repelling inner sheet S_r and a folded node on F^-. GSPT predicts here either MMO or RO in the full system, depending on the global return mechanism.[5,6] Specifically, we expect that the attractor will be a MMO periodic orbit, provided the passage near the folded node leads to a global return into the funnel region; this is precisely what happens for the case shown in Fig. 4. Detailed calculations shown in Fig. 7 of Ref. 11 provide ϵ-dependent boundaries of the MMO regime. In the case $\epsilon = 0.01$, this is given by $0.158 < \hat{\nu} < 0.259$ ($0.38 < \nu < 0.63$). For larger values of $\hat{\nu}$, the return is outside the funnel and the attractor will be a periodic orbit of ordinary RO type.

The type of attractor that occurs in the class I Atri model without pulsing is qualitatively the same for any sufficiently small value of ϵ, i.e., the attractor is either a stable node, a MMO or a RO, with the boundaries of the intervals of $\hat{\nu}$ on which each type of attractor occurs being only slightly changed by the size of ϵ. For example, the shift of the parameter value on the lower boundary of the MMO regime from its singular limit value is $O(\epsilon)$ and is explained by singular Hopf bifurcation theory.[16] On the other hand, the upper boundary of the MMO regime shifts from its singular limit value by $O(\epsilon^{1/2})$, as expected from canard theory.[5] A more quantitative underpinning, such as higher-order asymptotic estimates of these boundary shifts, is outside the scope of this work and will be reported elsewhere.

B. Class I dynamics with pulsing

The insight gained from the analysis of the unpulsed class I model yields an explanation for the different types of transient responses seen in the pulsed class I Atri model. Note that the long-term behavior of the pulsed model is just as for the unpulsed model, i.e., equilibria, MMOs, or ROs may be observed, depending on the sizes of $\hat{\nu}$ and ϵ.

The effect of a pulse of IP_3 is to send an orbit rapidly to a high value of P with the precise location after the pulse depending on the pulse size and on the position of the orbit immediately before the pulse. Since the evolution of P is independent of the other variables in the class I model, the P-component of the orbit will then relax to its equilibrium value, but during this relaxation the other variables will evolve in a more complicated way. The left column of Fig. 5 shows three different possibilities, corresponding to three representative values of $\hat{\nu}$; the corresponding panels in the right column are enlargements of the subthreshold phenomena occurring after the pulse is applied. The pulse response in Fig. 5(a), for $\hat{\nu} = 0.4$ ($\nu = 0.96$), exhibits a small transient increase in the frequency of oscillation, followed by smooth re-establishment of the attracting RO. The transient phenomena are all of RO type [see Fig. 5(b)]. We observe a small
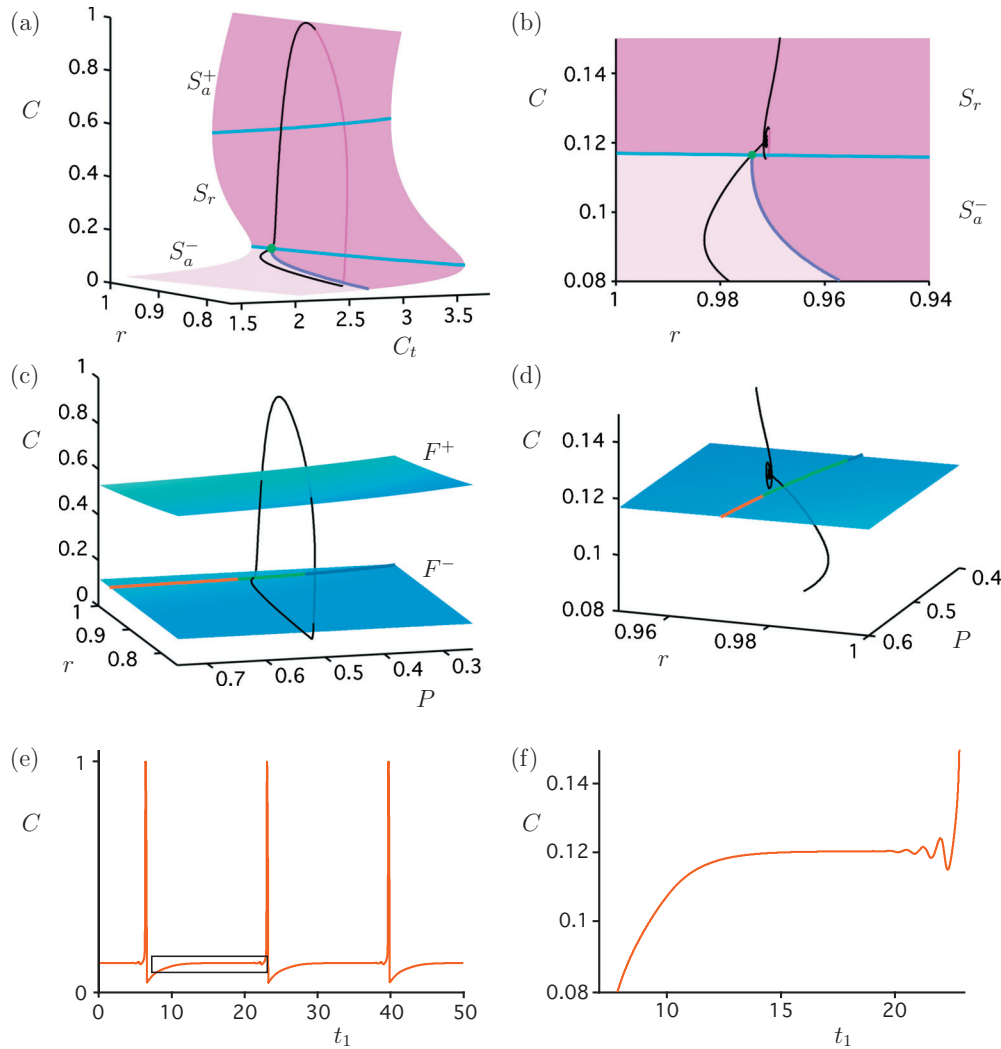
FIG. 4. (Color) Example of an attracting MMO (black curve) for the class I Atri model with $\epsilon=0.01$ and $\hat{\nu}=0.167$ ($\nu=0.40$). Panel (a) shows the intersection of the critical manifold (pink surface) with the slice in (C,r,C_t)-coordinates, where $P=\hat{\nu}/\hat{\beta}=0.50$ is fixed at its equilibrium value; the light pink section indicates the funnel region of the folded node (green dot) that occurs for this value of P. The blue curves are the intersections of the fold surfaces with the slice. Panel (b) is an enlargement showing the passage of the MMO past the folded-node singularity projected onto the (r,C)-plane. Panel (c) shows the projection onto (P,r,C)-coordinates with an enlargement near the folded node shown in panel (d). The blue surfaces are the fold surfaces $F^{\pm}$; on these surfaces the C_t-coordinate appears as a color gradient (light to dark as C_t increases). The red, green, and dark-blue curve is the locus of folded singularities; red indicates a folded saddle, blue indicates a folded focus, and green indicates a folded node, consistent with the color coding of singularities in Fig. 3. Panel (e) with corresponding enlargement in panel (f) shows the time series for C corresponding to the MMO.

decrease in oscillation amplitude immediately after the pulse is applied, caused by the fact that the transient orbit passes through a region of phase space in which the fold surfaces are closer together [see Fig. 6(a)]; this effect would not be detectable experimentally. Figure 5(c) shows the response for $\hat{\nu}=0.317$ ($\nu=0.76$). Here, we observe MMO-like behavior that causes relatively long delays between peaks during the transient part [see Fig. 5(d)]. Eventually, however, the orbit settles back to the expected RO for this $\hat{\nu}$-value. The response in Fig. 5(e) for $\hat{\nu}=0.233$ ($\nu=0.56$) relaxes back to an MMO, as expected, but we observe a very long delay before the oscillation restarts [see Fig. 5(f)].

The full three-dimensional critical manifold S_0 plays an important role in our explanation of the pulse response of the class I Atri model, as do the two-dimensional fold surfaces

and the curves of folded singularities. We already introduced these structures in the previous section and refer, in particular, to Fig. 3, where the three cases corresponding to Fig. 5 are indicated by white dashed vertical lines at the respective $\hat{\nu}$-values. Since P is no longer fixed for the pulsed class I Atri model, we always show in the figures that follow two projections, namely, one onto (C,r,C_t)-space and one onto (C,P,r)-space. In each projection we also plot the two fold surfaces $F^{\pm}$ with the curve of folded singularities of S_0. The fourth missing coordinate in each projection is indicated by a color gradient on the fold surfaces. We use light (low) to dark (high) for C_t, as before, and pink (high) to cyan (low) for P.

After the pulse, the orbit will typically not be near S_0 and the first behavior observed is, therefore, typically a fast tran-
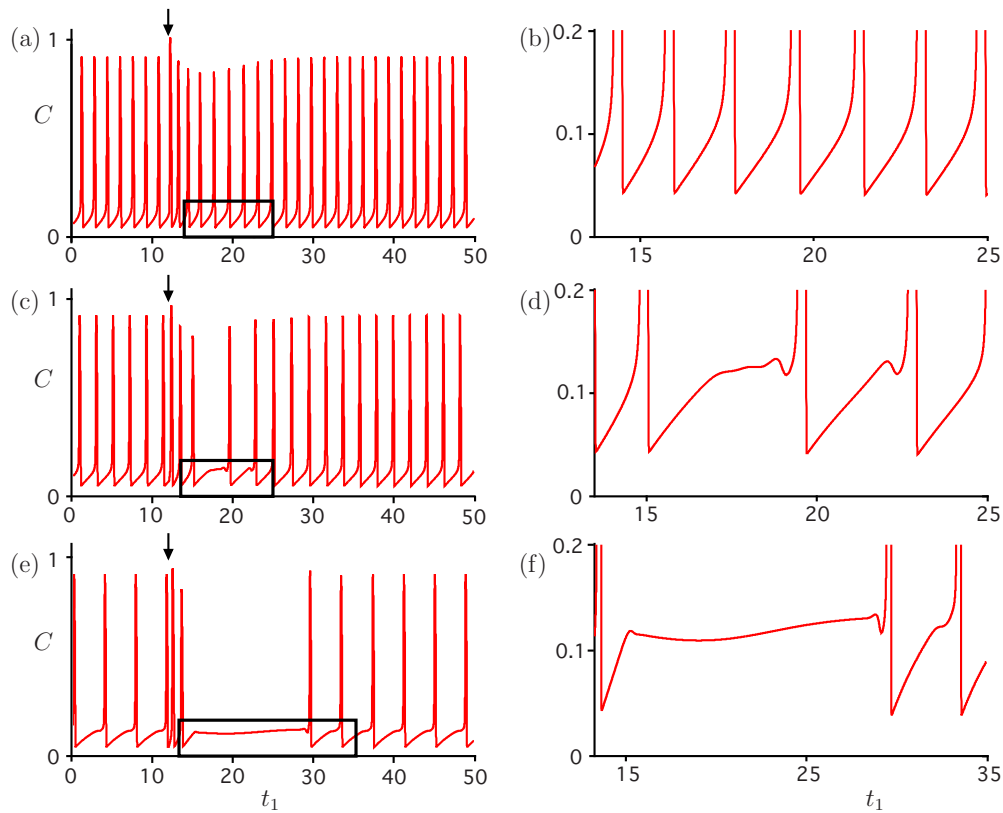
FIG. 5. (Color online) Time series of the C-coordinate for the pulsed class I Atri model with $\epsilon=0.01$. Panels (a), (c), and (e) show the responses for $\hat{\nu}=0.400$ ($\nu=0.96$), $\hat{\nu}=0.317$ ($\nu=0.76$), and $\hat{\nu}=0.233$ ($\nu=0.56$), respectively; these values correspond to the white dashed vertical lines in Fig. 3. Enlargements of the boxed regions in panels (a), (c), and (e) are given in panels (b), (d), and (f), respectively. These enlargements show the transient behavior after the pulse is applied at $t_1=12$ and P has decayed to 5. Compare also Figs. 6, 7, and 9.

sition to an attracting sheet of S_0, after which the evolution is (approximately) dictated by the slow flow on S_0 until the orbit meets a fold surface. This typically occurs at a regular jump point so that the orbit continues with a fast jump to the other attracting sheet of S_0. As a consequence, we observe a large RO in the transient dynamics.

We observe a series of such transient oscillations in the time series in Figs. 5(a) and 5(b), where $\hat{\nu}=0.4$ ($\nu=0.96$). The corresponding phase portrait is shown in Fig. 6; panel (a) shows the projection onto (C,r,C_t)-space and panel (b) onto (P,r,C)-space. Note that the curve of folded singulari-

ties consists only of folded foci (blue) for this $\hat{\nu}$-value (see Fig. 3). Fold points in a neighborhood of a folded focus are regular jump points. Hence, each time the fold surface is reached near such a folded focus a regular fast jump happens. By identifying the near-vertical transitions from the fold surface F^- in Fig. 6, we can identify the sequence of jump points on this fold surface. Both for the transient and the long-term dynamics, we see that the orbit interacts with the fold surface F^- at regular jump points and the oscillations are all of RO type.
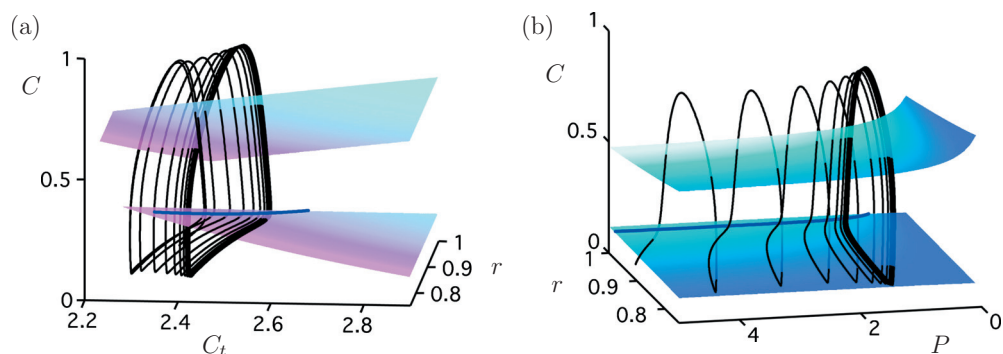

FIG. 6. (Color) RO-like transient behavior for the pulsed class I Atri model with $\hat{\nu}=0.4$ ($\nu=0.96$) and $\epsilon=0.01$. Panels (a) and (b) show projections onto (C_t,r,C)-space and (P,r,C)-space, respectively. The two fold surfaces are shown, with a color gradient indicating the value of the missing fourth coordinate; P ranges from 5 (pink) to 0 (cyan) in panel (a) and C_t ranges from 2.1 (light) to 3.2 (dark) in panel (b). The curves of folded singularities are also shown, with the color indicating the type of folded singularity as in Fig. 3. The corresponding time series for the orbit is shown in Figs. 5(a) and 5(b).
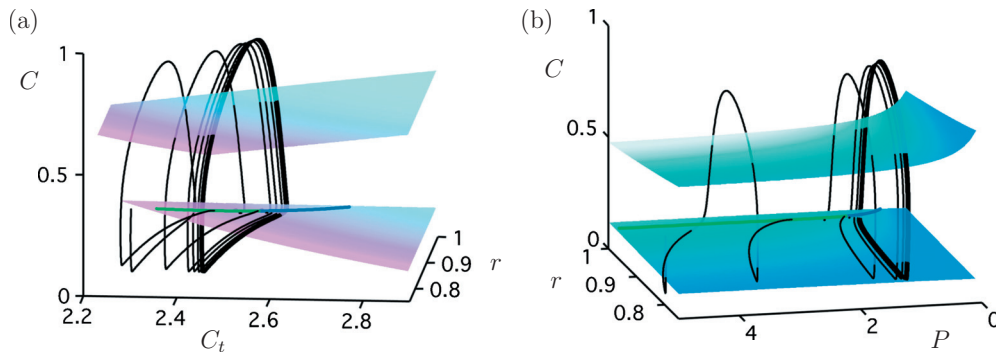
FIG. 7. (Color) MMO-like transient behavior for the pulsed class I Atri model with $\hat{\nu}=0.317$ ($\nu=0.76$) and $\epsilon=0.01$. Panels (a) and (b) show projections onto (C_t,r,C)-space and (P,r,C)-space, respectively. The two fold surfaces and folded singularities are shown with coloring as in Fig. 6. The corresponding time series for the orbit is shown in Figs. 5(c) and 5(d).

1. Anomalous delay due to interaction with a folded node

The time series in Fig. 5(c), where $\hat{\nu}=0.317$ ($\nu=0.76$), shows oscillations immediately after the pulsing similar to the case shown in Fig. 5(a), but the initial increase in frequency is followed by a relatively long delay before the orbit returns to its unpulsed oscillation, which is of RO type for this $\hat{\nu}$-value. Note the small-amplitude oscillations visible in the enlargement in Fig. 5(d) before the second and third spikes. As indicated in Fig. 3, the folded singularities on S_0 are no longer all folded foci. For high P-values, the singularities are folded nodes and there is an associated three-dimensional funnel region on S_0. As P decreases from a high value after pulsing, the transient orbit may enter this funnel region, in which case the orbit will have a quiescent period as it moves through the funnel region on S_a^- toward the curve

of folded-node singularities on F^-, then will exhibit small oscillations near F^- followed by a fast jump toward S_a^+. The transient orbit may return to the three-dimensional funnel region and again pass through another folded node at a smaller value of P, until P has decreased to values where the funnel ceases to exist because the folded singularities are of folded-focus type.

Figure 7 shows two projections of the phase portrait for the case with $\hat{\nu}=0.317$ ($\nu=0.76$). The MMO-like transient behavior occurs each time the orbit reaches the fold surface F^- at a (green) folded node. We observe that the pulsed orbit first crosses the fold surface F^- at a jump point, but after the fast jump, the orbit falls into the funnel region for the segment of folded-node singularities and the second crossing of the fold surface F^- is at a folded node.
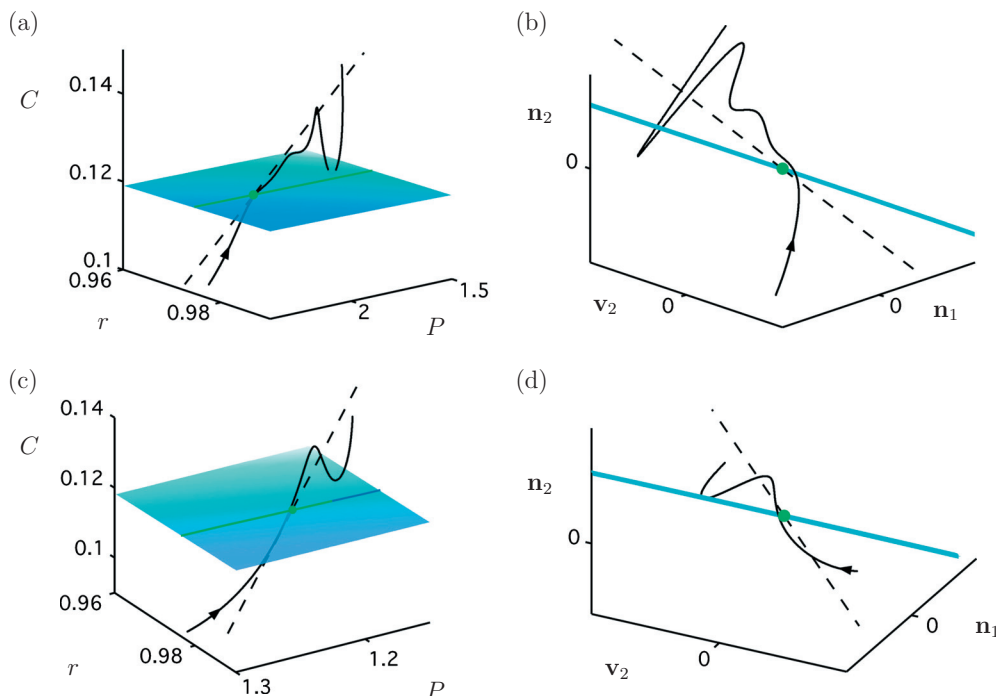

FIG. 8. (Color) Enlargements of segments of the pulsed orbit plotted in Fig. 7(b) near the second (a) and third (c) crossing of the fold surface F^- show the interaction with the curve of folded nodes. The black dashed lines are the weak eigenvectors of the folded nodes involved (green circles). The second column shows a projection along the vector direction associated with the zero eigenvalue of the folded node, such that the fold surface is almost one dimensional.
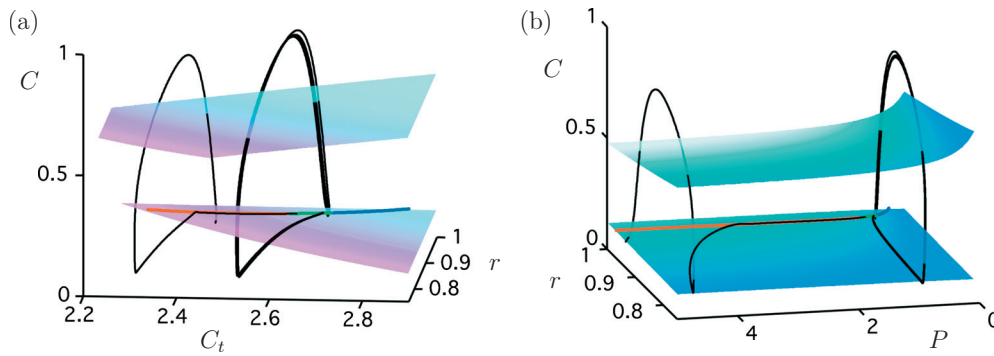
FIG. 9. (Color) Dynamics of the pulsed class I Atri model with $\hat{v}=0.233$ ($v=0.56$) and $\epsilon=0.01$, showing one orbit after pulsing (black curve). Panels (a) and (b) show projections onto (C_t, r, C)-space and (P, r, C)-space, respectively. At the equilibrium value of P, the folded singularity is a folded node. All surfaces and curves are colored as in Fig. 6. The corresponding time series for the orbit is shown in Figs. 5(e) and 5(f).

Panels (a) and (b) in Fig. 8 show a close-up of the passage through the folded-node segment at this second crossing; panel (a) is an enlargement near the folded node in the same projection as Fig. 7(b), and panel (b) shows the projection along the vector $\mathbf{v}_1$ associated with the zero eigenvalue of the folded node involved in this second crossing. The coordinate axes are aligned with the vector $\mathbf{v}_2$ that is tangent to the fold surface but orthogonal to $\mathbf{v}_1$, and with two additional vectors $\mathbf{n}_1$ and $\mathbf{n}_2$ normal to the fold surface. The projection in Fig. 8(b) shows oscillating behavior that is reminiscent of a passage through a folded node for a three-dimensional system with two slow variables.[5,6,26] Indeed, the small-amplitude oscillations occur about an axis that corresponds to the weak eigendirection of the folded node, which is the black dashed line in Fig. 8.

The third crossing of the fold surface by the orbit in Fig. 7(b) is also at a folded node. A close-up for this crossing is shown in Fig. 8(c), with Fig. 8(d) showing the projection along the vector associated with the zero eigenvalue. After this third crossing, P has decreased so much that the type of folded singularities changes to folded foci (blue segment) and the transient orbit (as well as the long-term behavior) thereafter looks like a RO.

The pulse response of the model at this value of $\hat{v}$ can, therefore, be characterized as being a few RO-type oscillations of greater frequency and smaller amplitude than the attracting RO, followed by a number of MMO-like oscillations (each including a delay, then some small-amplitude oscillations, then a fast jump) before re-establishment of the RO. We note that the number and amplitudes of the ROs immediately after the pulsing and before the delay, as well as the length of the delay and the number of small-amplitude oscillations during the transient, may depend on factors such as the location in phase space of the orbit immediately before pulsing, the length and magnitude of the applied pulse and on the exact $\hat{v}$ value, but the underlying mechanism described here is robust.

Thus, we have identified a mechanism causing anomalous delays in the pulse response of the class I Atri model: a "delay" before resumption of ROs can occur as the transient orbit after a pulse passes through the funnel region associated with a segment of folded-node singularities on the stable sheet S_a^- of the critical manifold. Note that the trapping region of the folded-node segment, the funnel, causes a delay effect because orbits on S_a^- slow down as they move to and along the weak eigendirection of the folded nodes. Furthermore, orbits have to make a certain number of small-amplitude oscillations near the folded nodes before they ultimately get "ejected" from the funnel.

2. Anomalous delay due to interaction with a segment of folded saddles

The anomalous delay seen in the time series in Fig. 5(e) is a pulse response of the class I Atri model that is caused by a second different mechanism, namely, by passage near a segment of folded-saddle singularities. We have found that a one-dimensional family of folded saddles can also provide a trapping region for the slow flow. Such a trapping region is bounded by the families of stable and unstable manifolds of the folded saddles. Unlike the funnel region for a segment of folded nodes, the families of (un)stable manifolds each form two-dimensional surfaces on S_a^- that prevent orbits from reaching the fold surface F^- and ultimately force solutions away from F^- on S_a^-. The unstable manifolds are often compact on S_a^- because they can bend back and connect to folded nodes in a neighboring segment. This offers an escape from the trapping region because solutions will leave a neighborhood of the folded saddles along the unstable eigendirection of the folded saddles until P eventually gets small enough that the folded singularities change to folded-node type. As soon as the orbit escapes from its "trap," a jump is observed in the transient orbit.

An example of this type of behavior is shown in Fig. 9 for the case $\hat{v}=0.233$. Both projections show that the pulsed orbit passes near F^-, lingering very close to the segment of folded saddles. Figure 10 shows an enlargement of part of Fig. 9(b), but projected onto (P, r, C)-space so that F^- appears horizontal. This figure also shows the two-dimensional surfaces formed by the one-dimensional stable (blue) and one-dimensional unstable (red) manifolds of the segment of folded saddles. The pulsed orbit enters this region near the surface of stable manifolds. As it comes close to the fold surface F^- and the curve of folded saddles, it is pushed away along the surface of unstable manifolds and remains trapped on S_a^- until it reaches the segment of folded nodes. Note that passage near a segment of folded saddles followed by a seg-
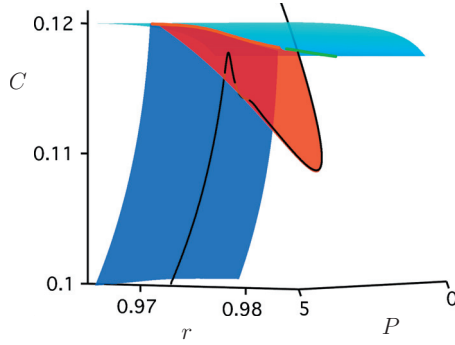
FIG. 10. (Color) Enlargement of Fig. 9, showing the stable (dark-blue) and unstable (dark-red) manifolds of the curve of folded saddles, as well as the pulsed orbit (black) as it passes through this region. The stable and unstable manifolds and the fold surface (light blue) all intersect at the curve of folded singularities (shown in light red and green).

ment of folded nodes produces a more lengthy delay than passage near a segment of folded nodes only. In this model, that delay is especially long as the unstable eigenvalues are very close to zero for the whole segment of folded saddles, meaning that solutions on the unstable manifold of the segment of folded saddles will stay close to the segment and, consequently, travel very slowly and take a long time to reach the folded-node region where oscillations resume.

III. DYNAMICS OF THE CLASS II MODEL

A class II model is defined as Eq. (1) with $\alpha \neq 0$ (here we choose $\alpha = 1.0$) and $0 < \hat{\tau} \ll 1$. Hence, the r-dynamics is considered fast, which leads to a model with two fast (C, r) and two slow variables (C_t, P). As explained in Ref. 11, it is possible to make a quasi-steady-state approximation of the r-variable by letting $\hat{\tau} \to 0$ and setting

$$r(C) = \frac{k_2^2}{k_2^2 + C^2},$$

in which case system (1) effectively becomes three dimensional, with one fast variable and two slow variables,

$$\begin{cases} \epsilon \dot{C} = \bar{J}_{\text{release}} - \bar{J}_{\text{serca}} + \epsilon(\bar{J}_{\text{in}} - \bar{J}_{\text{pm}}) =: \widetilde{f}(C, C_t, P, \epsilon) \\ \dot{C}_t = \bar{J}_{\text{in}} - \bar{J}_{\text{pm}} = g_1(C) \\ \dot{P} = \hat{\nu}\left(1 - \frac{1}{1 + C/k_4}\right) - \hat{\beta}P =: g_3(C, P). \end{cases} \quad (8)$$

Standard techniques from GSPT were used in Ref. 11 to analyze this system, and the main results from that paper are summarized in Sec. III A.

A. Class II dynamics in the absence of pulsing

The constraint $\widetilde{f}(C, C_t, P, 0) = 0$ defines the critical manifold S_0 of system (8). The constraint equation can be solved for C_t as a function of C and P; the resultant surface is plotted in Fig. 11. An important feature of S_0 is that it has two fold curves (relative to C) for $P < 0.45$, with the folds merging in a cusp at $P \approx 0.45$. In the region $P < 0.45$, the manifold is cubic shaped, with the outer sheets $S_a^{\pm}$ of S_0 (corresponding to larger and smaller values of C) being attracting and the inner sheet S_r (corresponding to intermediate values of C) being repelling. For $P > 0.45$, the single sheet S_a of S_0 is attracting. As usual, the critical manifold can be thought of as organizing the dynamics of Eq. (8) in the sense that, for sufficiently small ϵ, solutions of Eq. (8) will alternate between spending relatively long periods of time near S_0 and making fast jumps between different sheets of S_0.

As discussed in Ref. 11, for most values of $\hat{\nu}$ in the interval [0.311, 0.629] solutions are attracted to a RO like that shown in Fig. 11. This is the case even though there are folded-node singularities on the fold curves of S_0 because the global dynamics forces orbits away from the regions near the folded singularities. For ϵ sufficiently small, there can be a very small interval of $\hat{\nu}$ near $\hat{\nu} = 0.629$ where orbits are attracted to a folded node and MMOs are observed, but this is of no further interest here. Outside the interval [0.311, 0.629], solutions are attracted to a stable node.

For the purposes of understanding the response of the class II model to IP$_3$ pulses, a little more detail about the folded-node singularities is helpful. This detail does not affect the long-term behavior of solutions to this model but does have implications for the transient behavior immediately after a pulse, as discussed in Sec. III B. Figure 12
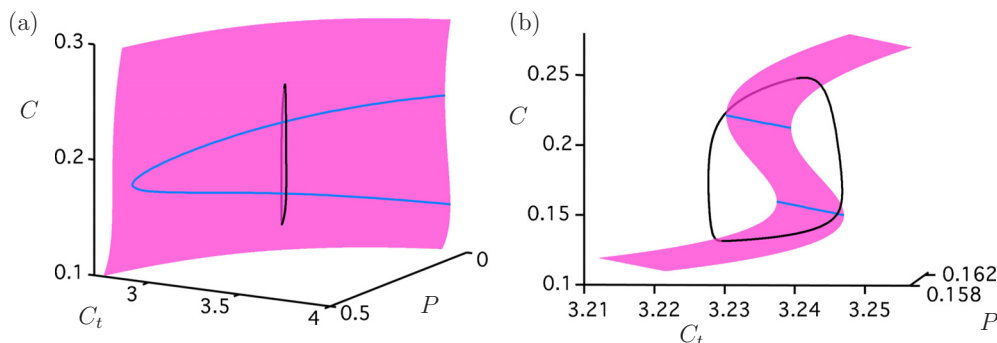

FIG. 11. (Color online) Example of an attracting RO (black curve) for the class II Atri model (8) with $\epsilon = 0.001$ and $\hat{\nu} = 0.417$ ($\nu = 1.0$). Panel (a) shows the critical manifold (pink surface), which has two fold curves for $P < 0.45$ (blue curves). These curves merge in a cusp point at $P \approx 0.45$. Panel (b) is an enlargement of panel (a) from a different view point, illustrating the cubic shape of the critical manifold.
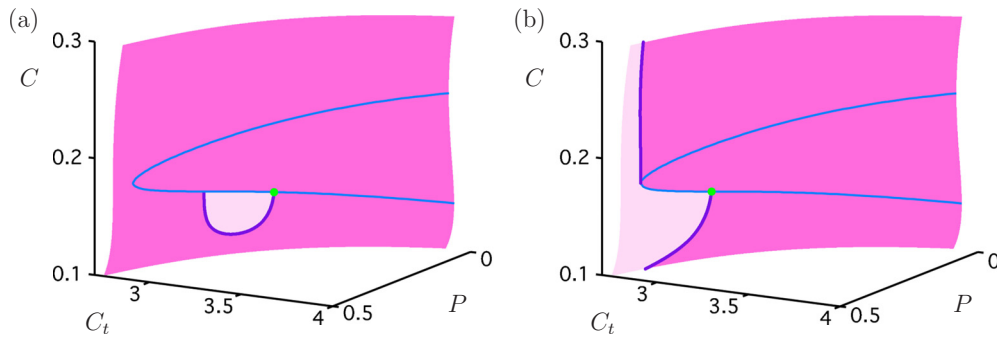
FIG. 12. (Color online) Dynamics on the critical manifold for the class II Atri model (8) for two values of $\hat{\nu}$: $\hat{\nu}=0.417$ ($\nu=1.0$) and $\hat{\nu}=0.542$ ($\nu=1.3$) in panels (a) and (b), respectively. The critical manifold is pink and the fold curves are blue. The green dots show the location of folded-node singularities and the purple curves emanating from the folded nodes are the associated strong canards. The light-pink region is the funnel region for the folded node. In panel (a), the funnel region is bounded by the lower fold curve and the strong canard. In panel (b), the funnel region is an open region of the critical manifold.

shows some features of the critical manifold for two representative choices of $\hat{\nu}$. For $\hat{\nu} \in [0.311, 0.446]$, the strong canard for the folded node on the lower fold curve bends around and joins again to the fold curve, meaning that the folded node is inaccessible unless an orbit starts in the funnel region which is bounded by the strong canard and the fold curve. This situation is illustrated in Fig. 12(a). In contrast, for $\hat{\nu} \in [0.446, 0.629]$, the strong canard does not meet the lower fold curve except at the folded node, and the associated funnel region is open. In this case, the funnel region attracts the flow from an open region of the critical manifold [see Fig. 12(b)].

B. Class II dynamics with pulsing

Due to the three-dimensional nature of the class II system, any delays such as that seen in Fig. 1(c) must be explained by a completely different mechanism than those used for the class I model. Nevertheless, we can still use the geometric structures found in the analysis of the unpulsed class II system. An IP$_3$ pulse applied to this model moves an orbit rapidly to higher values of P (i.e., past the cusp). For small ϵ, orbits will first move quickly toward the critical manifold, then follow the slow flow on the critical manifold until a fold curve is encountered, after which the orbit could make a fast jump. Since there are no folds in the critical manifold for

large P, there can be no fast jumps and hence no oscillations initially. Eventually, the value of P will decrease sufficiently that the orbit returns to the folded section of the critical manifold and then eventually to the attracting RO which occurs for low values of P. This explains the observed delay in the onset of oscillations after the pulse—until P is small enough there can be no oscillations.

The details of the evolution once P is small enough for the critical manifold to be folded ($P<0.45$) depend on the details of the folded singularities described above. For $\hat{\nu}<0.446$ ($\nu<1.07$), the funnel region (when it exists at all) is completely bounded by the fold curve and strong canard, and so a transient orbit cannot enter the region. Instead, the pulsed orbit goes below the funnel region and settles down to the RO. On the other hand, if the funnel region is open ($0.446<\hat{\nu}<0.629$, i.e., $1.07<\nu<1.51$), then a pulsed orbit will typically return to the attractor via the funnel of the folded node. This results in small oscillations in the transient orbit before RO are established again. Figure 13 confirms this prediction in the case $\hat{\nu}=0.542$ ($\nu=1.30$).

IV. DYNAMICS OF THE HYBRID MODEL

The hybrid Atri model is obtained by setting $\alpha \neq 0$ and $\tau \neq 0$ in Eq. (1). This system may have either two fast and two slow variables or one fast and three slow variables, de-
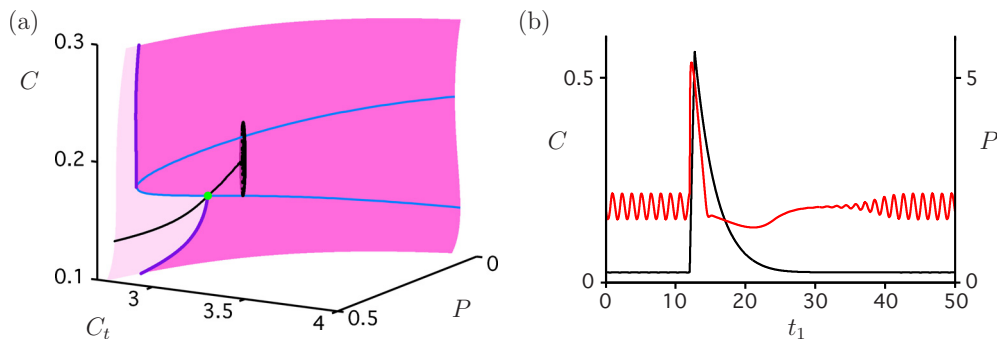

FIG. 13. (Color online) Dynamics for the class II Atri model (8) with $\hat{\nu}=0.542$ ($\nu=1.3$) and $\epsilon=0.01$. All curves and surfaces in panel (a) are the same as in Fig. 12, except that the black curve shows a trajectory after the application of an IP$_3$ pulse. After the pulse, the trajectory passes the cusp point on the fold curves, then passes through the funnel region toward the folded node, resulting in a delay followed by characteristic small oscillations before re-establishment of the RO. Panel (b) shows the corresponding time series of this trajectory. The red curve shows C and is plotted against the left vertical axis. The black curve is P and is plotted against the right vertical axis.
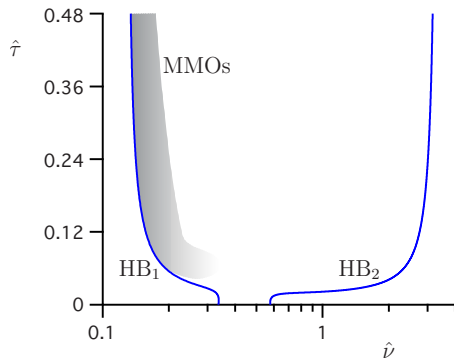
FIG. 14. (Color online) Partial bifurcation set for the hybrid Atri model (1) for $\epsilon = 0.01$, $\alpha = 1.0$, and various $\hat{\nu}$ and $\hat{\tau}$. The locations of Hopf bifurcations (HBs) are marked, and the shaded region indicates the values of $\hat{\nu}$ and $\hat{\tau}$ for which MMOs are observed. A sharp transition in the slope of the Hopf bifurcation curves occurs at $\hat{\tau} \approx 0.05$ at about the same value of $\hat{\tau}$ where MMOs cease to exist. This value of $\hat{\tau}$ corresponds to the hybrid model making a transition from having three slow variables ($\hat{\tau} = O(1)$) to having two slow variables ($\hat{\tau} = O(10^{-2})$).

FIG. 15. (Color) The types of folded singularity seen in the hybrid Atri model (1) with $\alpha = 1.0$, $\hat{\tau} = 0.48$ ($\tau = 2.0$), and $\epsilon = 0$ for a range of values of $\hat{\nu}$. The meanings of the colors are the same as in Fig. 3. The white dashed lines indicate the values of $\hat{\nu}$ used for Figs. 18–20. The black dashed curves (labeled P_{osc}) for $\hat{\nu} > 0.125$ indicate the maximum and minimum values of P for the attracting closed orbit (MMO or RO) at each value of $\hat{\nu}$. For $\hat{\nu} < 0.125$, the attracting orbit is an equilibrium solution with P value given by the dashed black line. The inset shows an enlargement of the indicated region.

pending on the relative size of $\hat{\tau}$. A comprehensive analysis of the hybrid Atri model was not presented in Ref. 11 either for unpulsed or pulsed versions of the model since GSPT relevant to systems with three slow variables had not been developed when Ref. 11 was written. In this section, we argue that when $\hat{\tau} = O(1)$ the dynamics of the hybrid model has many qualitative features of the pure class I model. As a consequence, the pulse response of the hybrid model is, for these values of $\hat{\tau}$, similar to the pulse response of the class I model. In particular, the delay sometimes seen after pulsing of the hybrid model when $\hat{\tau} = O(1)$ can be attributed to the existence of segments of folded saddles and folded nodes in the singular limit of the hybrid model. If, on the other hand, $\hat{\tau} \ll 1$, the hybrid model behaves like a class II model in both the pulsed and unpulsed dynamics. There is an intermediate range of values of $\hat{\tau}$ where the hybrid model is in transition between class I and class II forms. In this transition regime, there are more than two time scales in the model since r evolves on a distinct time scale, between fast and slow. GSPT based on the assumption of there being just two distinct time scales in the model is unable to give clear predictions about the behavior in the model in this case, and numerical investigations indicate that for $\hat{\tau}$ values in this regime features of both class I and class II dynamics may be observed. For instance, immediately after pulsing, a transient orbit may undergo a few oscillations with a slightly increased frequency (like in a class I model), then have a lengthy delay while the orbit moves near a section of critical manifold in which there are no folds and no folded singularities (like in a class II model) before regular oscillations resume.

A. Hybrid model without pulsing

Analysis of the time scales of the Atri model presented in Ref. 11 showed that the hybrid Atri model might be expected to behave like a class I model if $\hat{\tau} = O(1)$, and like a class II model if $\hat{\tau} = O(10^{-2})$. Numerical evidence for a transition regime is contained in Fig. 14, which shows a partial
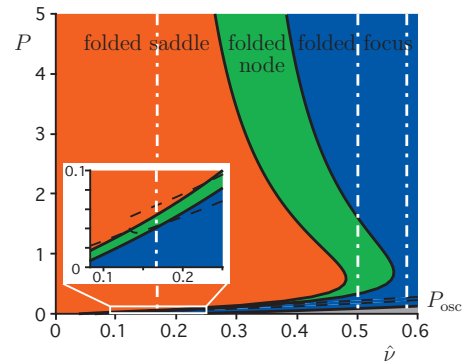
bifurcation set for the hybrid Atri model in the case that $\epsilon = 0.01$. Oscillations are possible only in the region in between the two curves of Hopf bifurcations, denoted HB$_1$ and HB$_2$ in Fig. 14. These oscillations are of RO type, except in the shaded region, where MMOs exist. A clear transition regime can be seen as $\hat{\tau}$ decreases in Fig. 14. Specifically, at $\hat{\tau} \approx 0.05$, the distance between HB$_1$ and HB$_2$ changes suddenly and the MMO regime terminates.

A detailed investigation of the case $\alpha = 1$, $\hat{\tau} = 0.48$ ($\tau = 2.0$), and $\epsilon = 0.01$, which is a representative parameter choice for which the hybrid model has three slow variables, provides evidence that there are many features in common between this model and the pure class I model discussed in Sec. III. In the hybrid model, P does not evolve independently of other variables, with the consequence that the long-term dynamics does not lie in fixed-P slices of phase space (as was the case for class I), but otherwise phase space plots look rather similar to Figs. 2, 4, and 6–9, as will be shown below.

Techniques from GSPT can be applied to the hybrid model, just as for the class I model in Sec. II. In particular, the three-dimensional critical manifold and the different types of folded singularities that exist can be computed, and singular MMOs can be constructed for a range of values of $\hat{\nu}$ where folded-node singularities occur. Figure 15 shows the types of folded singularity seen in the hybrid system for various values of $\hat{\nu}$. While the boundaries of the regions of existence of the various types of folded singularities have shifted compared with the class I case shown in Fig. 3, the similarities are clear. Note that in class I, the variable P evolves to a single equilibrium value, even if the other variables oscillate as part of a MMO or RO, whereas in the hybrid model, P oscillates slightly when there is a MMO or RO. The range of values of P that occurs along the singular closed orbit for each value of $\hat{\nu}$ is indicated by the dashed black curves labeled P_{osc} in Fig. 15.

The geometric structures present in the singular limit perturb in the nonsingular case just as they did for class I.
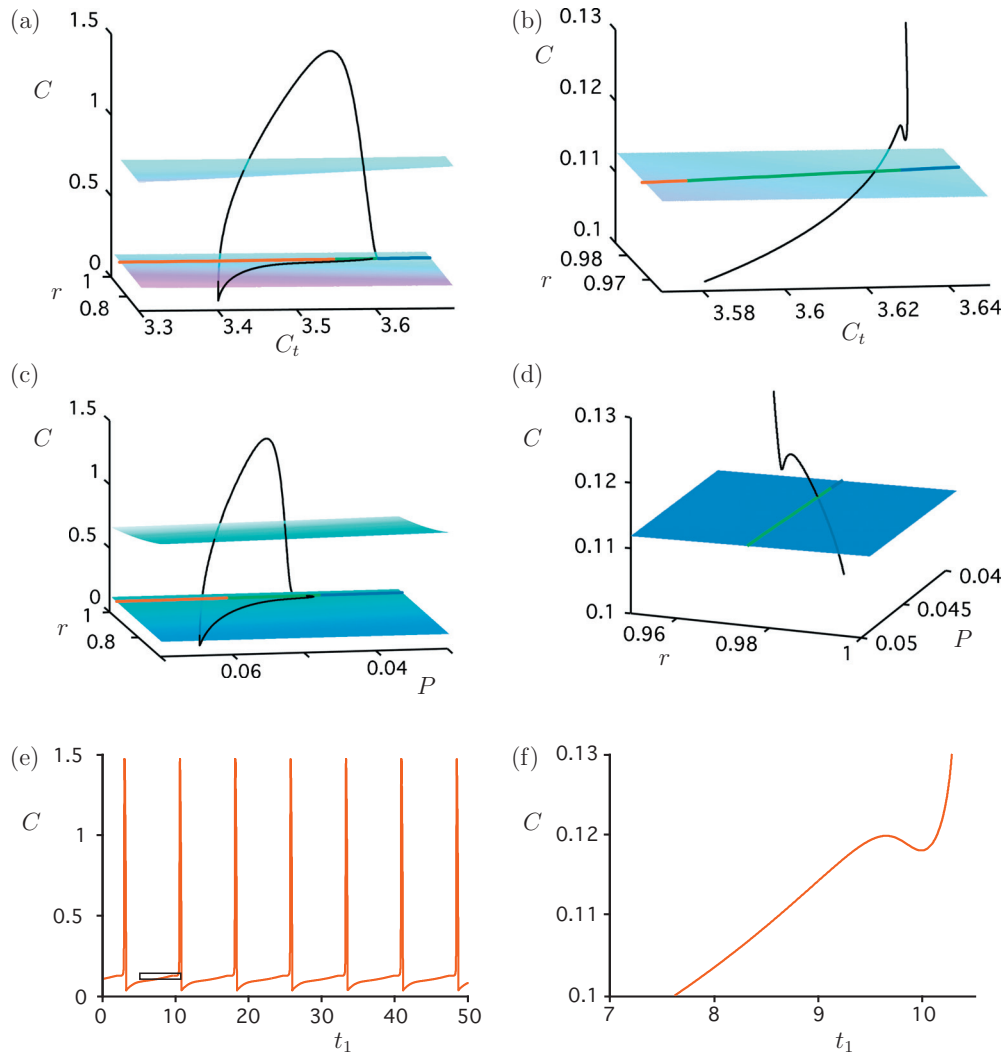
FIG. 16. (Color) Example of an attracting MMO (black curve) for the hybrid Atri model for $\epsilon=0.01$, $\alpha=1.0$, $\hat{\nu}=0.167$ ($\nu=0.40$), and $\hat{\tau}=0.48$ ($\tau=2.0$). Color coding of surfaces and curves is as in Fig. 6. Panel (a) shows a projection onto (C_t, r, C)-coordinates with an enlargement illustrating the passage of the MMO past the folded-node singularity in panel (b). Panels (c) and (d) similarly show the situation projected onto (P, r, C)-coordinates [compare with Figs. 4(c) and 4(d)]. Panel (e) with corresponding enlargement in panel (f) shows the time series for C corresponding to the MMO.

Thus, for instance, intervals of $\hat{\nu}$ for which singular MMOs or ROs occur in the singular limit persist in the nonsingular system, with the boundaries of these intervals shifted in an appropriate ϵ-dependent way, just as shown above for class I.

Figure 16 gives an example of class I-like behavior of the hybrid model, for the choice $\hat{\nu}=0.167$ ($\nu=0.40$); for this choice of parameters, there is an attracting MMO. There are clear similarities between Figs. 4 and 16, consistent with our claim that the hybrid Atri model behaves like a class I model when $\hat{\tau}=O(1)$.

The dynamics of the unpulsed hybrid model in the case that $\hat{\tau}=O(10^{-2})$ or less is qualitatively like the dynamics for the pure class II model, but the argument is simpler than for the class I case: the quasi-steady-state approximation used to reduce the class II model to a system of three equations in Ref. 11 works equally well for the hybrid model when $\hat{\tau}=O(10^{-2})$ or less, and so our description of the class II model dynamics in Sec. III is valid also for the hybrid model in this regime.

When $\hat{\tau}$ is of an order intermediate between $O(1)$ and $O(10^{-2})$, then methods of analysis based on the assumption of there being two distinct time scales in the model are no longer appropriate. Results derived for systems with three time scales may be relevant for this transition regime,[6,14] but we do not undertake this kind of analysis here.

B. Hybrid model with pulsing

Since the long-term dynamics of the hybrid model can be qualitatively like the dynamics in either the class I or class II models, depending on the size of $\hat{\tau}$, it is no surprise that the hybrid model may respond to a pulse of IP$_3$ in similar ways to the class I and II models. In particular, we may encounter the same types of anomalous delays as for class I. We illustrate this using the hybrid model with $\hat{\tau}=0.48$ ($\tau=2$) and $\epsilon=0.01$. Figure 17 shows three different possibilities, corresponding to three representative values of $\hat{\nu}$; compare with the pulsed responses for the class I model in Fig. 5.
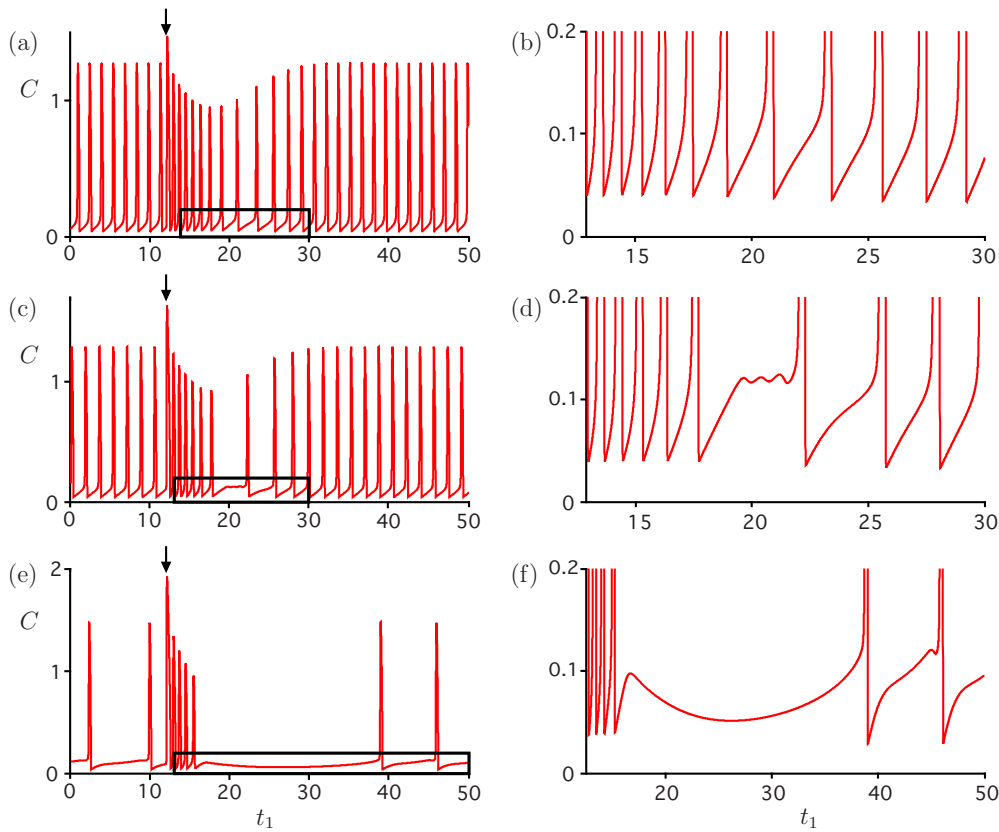
FIG. 17. (Color online) Time series of the C-coordinate for the pulsed hybrid Atri model with $\alpha=1.0$, $\hat{\tau}=0.48$ ($\tau=2.0$), and $\epsilon=0.01$. Panels (a), (c), and (e) show the responses for $\hat{\nu}=0.583$ ($\nu=1.4$), $\hat{\nu}=0.500$ ($\nu=1.2$), and $\hat{\nu}=0.167$ ($\nu=0.40$), respectively; these values correspond to the white dashed vertical lines in Fig. 15. Enlargements of the boxed regions in panels (a), (c), and (e) are given in panels (b), (d), and (f), respectively. These enlargements show transient behavior after the pulse is applied at $t_1=12$ and P has decayed to 5. Compare also Figs. 18–20.

Figure 18 shows a pulsed orbit in phase space for the hybrid model when $\hat{\tau}=0.48$ ($\tau=2$) and $\hat{\nu}=0.583$ ($\nu=1.4$), with the associated time series being plotted in Figs. 17(a) and 17(b). In this case, the unpulsed model is in the class I regime and we can locate a three-dimensional critical manifold containing a curve of folded singularities. The folded singularities consist of folded foci only and the pulsed orbit meets the fold surface F^- at jump points only. The pulse response for this value of $\hat{\nu}$ is, therefore, qualitatively similar to that seen in the class I model with $\hat{\nu}=0.400$ [see Figs. 5(a), 5(b), and 6].

Figure 19 shows a pulsed orbit for the hybrid model when $\hat{\nu}=0.500$ ($\nu=1.2$), with the associated time series being plotted in Figs. 17(c) and 17(d). In this case, the first four passages through the fold surface F^- occur at jump points, the next passage is at a folded node, and the orbit eventually settles down to a RO. The pulse response for this value of $\hat{\nu}$ is, thus, qualitatively similar to the case for the class I model with $\hat{\nu}=0.317$ [see Figs. 5(c), 5(d), and 7].

Figure 20 shows a pulsed orbit for the hybrid model when $\hat{\nu}=0.167$ ($\nu=0.4$), with the associated time series being plotted in Figs. 17(e) and 17(f). In this case, the pulsed orbit
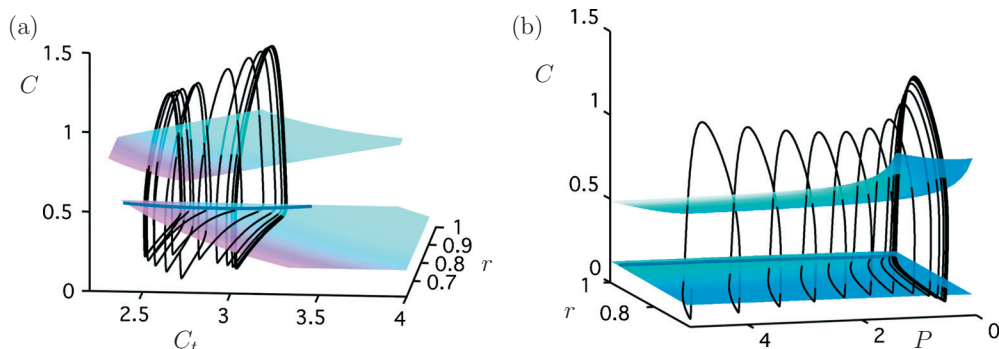

FIG. 18. (Color) RO-like transient behavior for the pulsed hybrid Atri model with $\hat{\nu}=0.583$ ($\nu=1.4$), $\alpha=1.0$, $\hat{\tau}=0.48$ ($\tau=2.0$), and $\epsilon=0.01$. Panels (a) and (b) show projections onto (C_t,r,C)-space and (P,r,C)-space, respectively. All surfaces and curves are the same as in Fig. 6. All intersections of the orbit with the fold surface occur at jump points. A time series for the orbit is shown in Figs. 17(a) and 17(b).
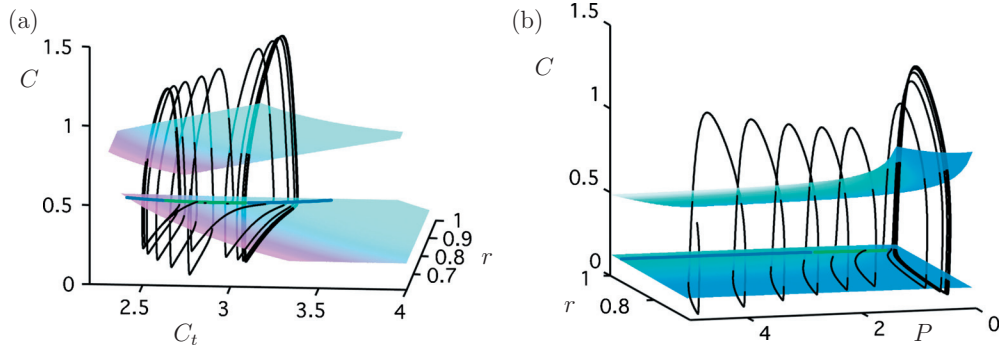
FIG. 19. (Color) MMO-like transient behavior for the pulsed hybrid Atri model with $\hat{\nu}=0.50$ ($\nu=1.2$), $\alpha=1.0$, $\hat{\tau}=0.48$ ($\tau=2.0$), and $\epsilon=0.01$. Panels (a) and (b) show projections onto (C_t,r,C)-space and (P,r,C)-space, respectively. All surfaces and curves are the same as in Fig. 6. The first five passages through the fold surface are at jump points, the next passage is at a folded node, and the orbit is eventually attracted to a RO (crossing the fold surface at a jump point). A time series for the orbit is shown in Figs. 17(c) and 17(d).

makes two passages through the fold surface F^- at jump points, then spends an extended period of time drifting near the segment of folded saddles, then enters the funnel region for the folded nodes, and eventually settles down to an MMO. The pulse response for this value of $\hat{\nu}$ is, thus, like the case for the class I model with $\hat{\nu}=0.233$ [see Figs. 5(e), 5(f), and 9].

Hence, we see that the hybrid Atri model with $\alpha=1.0$ and $\hat{\tau}=0.48$ ($\tau=2.0$) responds to pulses of IP$_3$ in a qualitatively similar way to the class I Atri model. Similar results are found for any $\hat{\tau}$ greater than about 0.2.

As argued above, when the hybrid model is in the class II regime, i.e., when $\hat{\tau}\ll1$, the model can be reduced to a three-dimensional model and we find in numerical experiments that pulsing has a similar effect to that seen in the pure class II model. Specifically, after pulsing, there is a delay before re-establishment of oscillations because the pulse pushes the orbit into a region of the phase space where the associated critical manifold has no folds. Oscillations are only re-established once the variable P has decayed enough that the critical manifold is folded.

We have derived no clear theoretical predictions about the response to pulsing for the hybrid model in the transition regime between the class I and class II regimes, but preliminary numerics show that in this case the pulse response has

characteristics of both class I and class II behavior. The transition regime is being investigated further and will be reported on elsewhere.

V. DISCUSSION

In this paper, we have used GSPT to investigate the response of a representative model (the Atri model) of oscillatory calcium dynamics to an exogenous pulse of IP$_3$. Previous work on this model[7] identified a so-called *anomalous delay* in the transient response of certain versions of the model, specifically in the class I and hybrid versions of the model for a range of values of the main bifurcation parameter $\hat{\nu}$, and gave a heuristic explanation for the phenomenon based on a fast-slow decomposition with one slow variable. However, as we have shown, a full analysis of pulsing in the Atri model requires recognition that the model may have two or three slow variables.

Making use of the recent results of Wechselberger,[25] which extend canard theory to systems with three or more slow variables, we have shown that the delays sometimes seen in the pulsed class I and hybrid versions of the Atri model are associated with the existence of a curve of folded singularities, either folded saddles or folded nodes, in the singular limit of the model. In the parameter regime of inter-
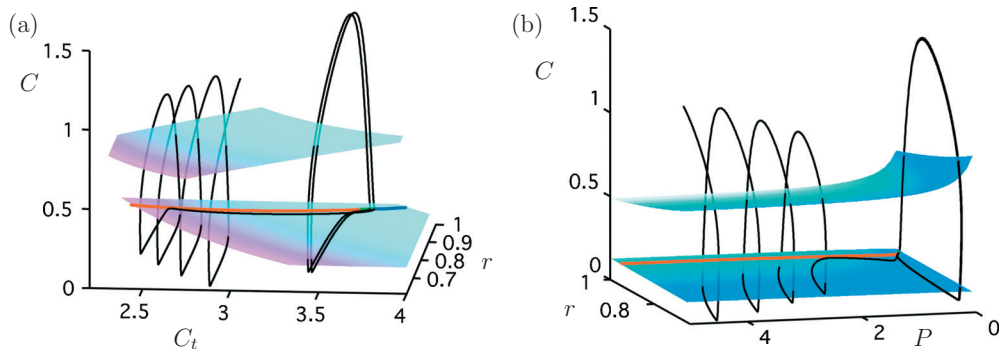

FIG. 20. (Color) Dynamics for the pulsed hybrid model with $\hat{\nu}=0.167$ ($\nu=0.4$), $\alpha=1.0$, $\hat{\tau}=0.48$ ($\tau=2.0$), and $\epsilon=0.01$. Panels (a) and (b) show projections onto (C_t,r,C)-space and (C,r,P)-space, respectively. All surfaces and curves are the same as in Fig. 6. The first three passages through the fold surface occur at jump points, then the orbit has a period of drifting along the curve of folded saddles. Eventually, the orbit settles down to an MMO, corresponding to passage near a folded node. A time series for the orbit is shown in Figs. 17(e) and 17(f).

est, the Atri model has periodic attractors, typically of either MMO or RO type. The effect of pulsing with IP$_3$ is to move the orbit rapidly away from the periodic attractor to a region of phase space where P is large. The way in which the orbit returns through phase space to the vicinity of the periodic attractor produces the characteristic pulse response of the model and is heavily influenced by the dynamics of the singular limit of the model of interest, as summarized below.

In the class I version of the Atri model, P evolves independently of the other variables. After pulsing, P decays monotonically to an equilibrium value, while the other variables can oscillate. For sufficiently small values of the singular perturbation parameter ϵ, the transient orbit will alternate between periods when it closely follows the critical manifold of the singular limit system and fast jumps between different sheets of the critical manifold. At larger values of $\hat{\nu}$ where the critical manifold either has no folded singularities or the folded singularities are of folded-focus type, then transient and long-term oscillations are of RO type; while the transient orbit might display small changes in frequency or amplitude of oscillation after pulsing, no significant delays are observed in the associated time series. However, at smaller values of $\hat{\nu}$ when the singular limit has folded singularities of folded-node or folded-saddle type, there may be relatively long periods in the transient orbit where there are no oscillations. Sometimes the transient orbit displays MMO-like behavior including delays and small-amplitude oscillations (when it passes near a segment of folded nodes) and sometimes there is a more lengthy delay (when the orbit passes near a segment of folded saddles), followed by MMO-like transients (near a segment of folded nodes).

Delays are also observed in the pulse response of the class II Atri model, but in this case they are caused by a completely different mechanism. We showed that in the parameter regime of interest, the two-dimensional critical manifold for the singular limit of the class II Atri model has a cusp; for smaller values of P, the critical manifold is cubic shaped, which means that ROs (and sometimes MMOs) can occur, but at higher values of P, the folds merge in a cusp so that the critical manifold is not folded and oscillations do not occur. The effect of pulsing in this case is to send the orbit into the part of phase space where the manifold is not folded. Until the variable P has decayed sufficiently so that the orbit has passed the cusp region and once again gets close to the folded part of the critical manifold, there can be no oscillations. This results in the observed delay in the onset of oscillations after pulsing in the class II model.

We have argued that the hybrid Atri model has three regimes: a class I regime when $\hat{\tau} = O(1)$, a class II regime when $\hat{\tau} = O(10^{-2})$ or less, and a transition regime for intermediate sizes of $\hat{\tau}$. The form of the pulse response of the hybrid model is then determined by these regimes: the pulse response is class I-like if the unpulsed model is in the class I regime and is class II-like if the unpulsed model is in the class II regime. Features of both class I and class II pulse responses can be seen in the hybrid model in the transition regime.

A crucial step in understanding the dynamics of the class I Atri model and of the hybrid model in the class I regime

was the ability to apply GSPT to systems with three slow variables. The examples in this paper are the first application of the results in Ref. 25 that extend canard theory to the case of three (or more) slow variables. Based on what is seen in systems with two slow variables,[5,6,23,26] it is perhaps not surprising that the presence of folded-node singularities in the singular limit of the Atri model can result in complicated (MMO-like) dynamics. More surprising is the important role played by folded saddles; we found that passage near a segment of folded saddles can result in an extended quiescent period in the time series of a pulsed solution. The trapping region created by the (un)stable manifolds of the folded saddles is only terminated due to a transition in the type of folded singularities—here to folded nodes—and the release is observed as a transient calcium spike due to a jump near a folded node. We note that a passage near a single folded singularity would not produce this effect; this is something that can only occur in systems with three or more slow variables.

A major difference between our analysis of the Atri model and that presented in Ref. 7 is that we have determined that the model can have two or three slow variables, whereas just one slow variable (c_t in the notation of Ref. 7) was used in Ref. 7. As a consequence, some features of the dynamics (such as MMOs) were not identified in Ref. 7. Analysis of the pulse responses for class I and hybrid models in Ref. 7 implicitly had two slow variables since p and c_t were treated as parameters, and an association between the location of certain bifurcations of the (two-dimensional) fast subsystem and the transient behavior of the pulsed orbits was reported. We believe that our use of a singular limit in which there are either three slow variables (for class I and some hybrid cases) or two slow variables (for class II and some hybrid cases) leads to a clearer explanation of the observed phenomena, including the long-term dynamics and the response to pulsing.

The original motivation for studying the response of the Atri model to a pulse of IP$_3$ was a desire to understand the dynamics behind an experimental protocol proposed in Ref. 22. In the models studied in Ref. 22, it seemed that there was a clear difference in the response of different types of model to an IP$_3$ pulse: class I models responded with a temporary increase in oscillation frequency, while class II models responded with a phase lag (delay) before re-establishment of oscillations. Thus, it was thought that the experimental protocol could be used to determine whether the calcium oscillations in a particular cell type were predominantly determined by class I or class II mechanisms. The anomalous delays that are sometimes observed when the class I Atri model is pulsed have muddled the presumed differences between the response types. In this paper, we have identified the mathematical mechanisms behind the varying types of pulse responses; the next steps are to look at other intracellular calcium models (see, e.g., Refs. 8, 17, and 18) to determine whether these mechanisms are present and then to revisit the experimental protocol to see if it can be modified so that its interpretation is unambiguous. Work along these lines is ongoing and will be reported elsewhere.

Finally, we note that identification of the time scales present in the Atri model suggests a mathematical basis for determining whether class I or class II mechanisms will drive the oscillations in a hybrid model that includes both. We conjecture that the dominant mechanism is determined by the relative speed of the receptor dynamics (represented by the variable r in our model); slow receptor dynamics will result in class I mechanisms being dominant and fast receptor dynamics will result in class II mechanisms being dominant. This insight into the behavior of hybrid models has been confirmed in this paper for the Atri model, but results for other models will be reported elsewhere.

ACKNOWLEDGMENTS

[1]Atri, A., Amundsen, J., Clapham, D., and Sneyd, J., "A single-pool model for intracellular calcium oscillations and waves in the Xenopus laevis oocyte," Biophys. J. **65**, 1727–1739 (1993).

[2]Benoît, E., "Systemes lents-rapides dans $\mathbb{R}^3$ et leurs canards," Troisième recontre du Schnepfenried, Vol. 109-110 of Astérisque (Soc. Math. France, Paris, 1983), pp. 159–191.

[3]Berridge, M. J., Bootman, M. D., and Lipp, P., "Calcium—A life and death signal," Nature (London) **395**, 645–648 (1998).

[4]Brøns, M., Kaper, T., and Rotstein, H., "Focus issue: Mixed mode oscillations: Experiment, computation, and analysis," Chaos **18**, 015101 (2008).

[5]Brøns, M., Krupa, M., and Wechselberger, M., "Mixed mode oscillations due to the generalized canard phenomenon," Fields Inst. Commun. **49**, 39–63 (2006).

[6]Desroches, M., Guckenheimer, J., Kuehn, C., Krauskopf, B., Osinga, H. M., and Wechselberger, M., "Mixed-mode oscillations with multiple time-scales," Bristol Centre for Applied Nonlinear Mathematics Preprint No. BCANM 1594, 2010.

[7]Domijan, M., Murray, R., and Sneyd, J., "Dynamical probing of the mechanisms underlying calcium oscillations," J. Nonlinear Sci. **16**, 483–506 (2006).

[8]Dupont, G. and Erneux, C., "Simulations of the effect of inositol 1,4,5-triphosphate 3-kinase and 5-phosphotase activities on Ca^{2+} oscillations," Cell Calcium **22**, 321–331 (1997).

[9]Ermentrout, B. and Wechselberger, M., "Canards, clusters and synchronization in a weakly coupled interneuron model," SIAM J. Appl. Dyn. Syst. **8**, 253–278 (2009).

[10]Fenichel, N., "Geometric singular perturbation theory for ordinary differential equations," J. Differ. Equations **31**, 53–98 (1979).

[11]Harvey, E., Kirk, V., Sneyd, J., and Wechselberger, M., "Multiple time scales, mixed mode oscillations and canards in models of intracellular calcium dynamics," 2010, http://www.maths.usyd.edu.au/u/wm/.

[12]Jones, C. K. R. T., "Geometric singular perturbation theory," *Dynamical Systems (Montecatini Terme, 1994)* (Springer-Verlag, Berlin, 1995).

[13]Keener, J. and Sneyd, J., *Mathematical Physiology*, 2nd ed. (Springer-Verlag, New York, 2008).

[14]Krupa, M., Popovic, N., and Kopell, N., "Mixed-mode oscillations in three time-scale systems: A prototypical example," SIAM J. Appl. Dyn. Syst. **7**, 361–420 (2008).

[15]Krupa, M., Popovic, N., Kopell, N., and Rotstein, H. G., "Mixed-mode oscillations in a three time-scale model for the dopaminergic neuron," Chaos **18**, 015106 (2008).

[16]Krupa, M. and Szmolyan, P., "Relaxation oscillation and canard explosion," J. Differ. Equations **174**, 312–368 (2001).

[17]Li, Y. and Rinzel, J., "Equations for InsP$_3$ receptor mediated $[Ca^{2+}]_i$ oscillations derived from a detailed kinetic model: A Hodgkin-Huxley like formalism," J. Theor. Biol. **166**, 461–473 (1994).

[18]Politi, A., Gaspers, L. D., Thomas, A. P., and Höfer, T., "Models of IP$_3$ and Ca^{2+} oscillations: Frequency encoding and identification of underlying feedbacks," Biophys. J. **90**, 3120–3133 (2006).

[19]Rotstein, H. G., Wechselberger, M., and Kopell, N., "Canard induced mixed-mode oscillations in a medial entorhinal cortex layer II stellate cell model," SIAM J. Appl. Dyn. Syst. **7**, 1582–1611 (2008).

[20]Rubin, J. and Wechselberger, M., "Giant squid—Hidden canard: The 3D geometry of the Hodgkin-Huxley model," Biol. Cybern. **97**, 5–32 (2007).

[21]Sneyd, J., Tsaneva-Atanasova, K., Yule, D. I., Thompson, J. L., and Shuttleworth, T. J., "Control of calcium oscillations by membrane fluxes," Proc. Natl. Acad. Sci. U.S.A. **101**, 1392–1396 (2004).

[22]Sneyd, J., Tsaneva-Atanasova, K., Reznikov, V., Bai, Y., Sanderson, M. J., and Yule, D. I., "A method for determining the dependence of calcium oscillations on inositol trisphosphate oscillations," Proc. Natl. Acad. Sci. U.S.A. **103**, 1675–1680 (2006).

[23]Szmolyan, P. and Wechselberger, M., "Canards in $\mathbb{R}^3$," J. Differ. Equations **177**, 419–453 (2001).

[24]Vo, T., Bertram, R., Tabak, J., and Wechselberger, M., "Mixed-mode oscillations as a mechanism for pseudo-plateau bursting," J. Comput. Neurosci. **28**, 443–458 (2010).

[25]Wechselberger, M., "A propos de canards (Apropos canards)," 2010, http://www.maths.usyd.edu.au/u/wm/.

[26]Wechselberger, M., "Existence and bifurcation of canards in $\mathbb{R}^3$ in the case of a folded node," SIAM J. Appl. Dyn. Syst. **4**, 101–139 (2005).